GEOTECHNICAL SITE INVESTIGATION USING SEISMIC REFRACTION AND RESISTIVITY TECHNIQUES

by

EMMANUEL TETTEH HUADJI, BSc(Hons)

A Thesis Submitted to the Department of Physics,

Kwame Nkrumah University of Science and Technology

in partial fulfillment of the requirements for the degree

of

MASTER OF PHILOSOPHY

College of Science

Supervisor: Prof. Sylvester K. Danuor

April 24, 2015

Declaration

I declare this submission is my own work towards the MPhil and that its content has no previously published materials by any other person except where it is duely acknowledged. It also contains no material accepted for the award of any other degree of the University.

.....	.....	.....
Student Name & ID (PG8045812)	Signature	Date

Certified by:

.....	.....	.....
Supervisor Name	Signature	Date

Certified by:

.....	.....	.....
Head of Dept. Name	Signature	Date

Abstract

2D siesmic refraction and electrical resistivity surveys have been conducted at the KNSUT Business School extension site to find out how suitable the subsurface is for building construction purposes. The survey focused on using resistivity and p-wave velocity values obtained from the subsurface at the study area to predict clay zones, voids, fissures and faults, depth to the bedrock and also examine the campaction of the weathered zone. Fourteen traverses each 240 m long oriented in the north to south with an inter-profile separations of 10 m were covered. Resistivity data were collected using the ABEM Terrameter SAS 4000 with the Wenner array and an electrode separation of 4 m. To cover the whole profile length, the roll-along technique was employed. Seismic data were collected using 10 Hz electromagnetic geophones with the ABEM Terraloc Mk.6, a 24 channel recording system. A full version of the RES2DINV software was used to obtain 2D inverse models of the resistivity data. The 2D resistivity data were collated and into 3D model of the subsurface. Seismic data was also processed with the ReflexW software into 2D velocity depth models unveiling three acoustic layers. P-wave velocity ranges of 699-870 m/s, 1189.1-1450.5 m/s and 3759-5321 m/s were recorded for the first, second and third layers respectively. The use of the 2D velocity depth models and the geoelectrical inverse models together with geologic information from the study area helped in the interpretations. Weak zones, distribution of the subsurface resistivity and possible voids were mapped with the resistivity method. The

seismic method delineated the bedrock at depths > 20 m at the north which becomes close to the land surface at about 13 m at the south with p-wave velocity > 3759 m/s. The north and east display a highly compact weathered layer that can hold the weight of buildings but the south and part of the west cannot support the weight of buildings due to a highly weathered subsurface with low degree of compaction.

Contents

List of Tables

List of Figures

List of Symbols

K	Bulk Modulus	∞	Infinity
μ	Shear Modulus	π	pi
V_p	Velocity of primary wave	ASL	Above Sea Level
V_s	Velocity of secondary wave		
i_c	Critical angle		
ρ_a	Apparent resistivity		
t_x	Arrival time of seismic waves at a receiver offset X from shot point		
t_i	Intercept time		
V_f	Seismic velocity in pore fluid.		
V_m	Seismic velocity in rock matrix.		
ϕ	Porosity		
V	Electrical potential		
R	Electrical resistance		
I	Electrical current		
J	Current density		
σ	Electrical conductivity		
E	Electric field intensity		
Ω	Ohm		

Acknowledgments

I would like to thank my parent for their prayers and support throughout my studies. To all my siblings most especially Mercy Paddy and Gladys Paddy I say God favour you in abundance.

My profound gratitude goes to my supervisor Prof. Sylvester Kojo Danuor, Mr. Van-Dycke Asare Sarpong and Mr. Thomas Dwomoh for their selfless support during data acquisition. Dr. A.A Aning is highly acknowledged for his advice and introduction to geophysical field work. I will be very ungratefull if I don't appreciate Mr. Ernest Ohene Asare for his kind support and tutorials on LaTeX.

All the following names are appreciated for their support on the field: Dorcas Attuabea Addo, Issahaku Jackalia Sontaa, Nathaniel Sackey, George Hinson, Obed Sedowua and Victor Mensah. God richly bless you.

CHAPTER 1

INTRODUCTION

1.1 Background

Geophysical techniques are widely known in every part of the globe for their outstanding role in the exploration of some natural resources such as gold, buaxite, diamond, copper, oil and gas and other minerals that the world can not live without. Geophysics is simply investigating the Earth's interior structure using the principles of physics.

Information from beneath the earth surface can be derived either by direct or indirect means. Topographic map interpretation, aerial photography and the study of existing geological reports, maps, and soil surveys indirectly provide subsurface information. Direct methods include drilling of boreholes from which disturbed and undisturbed samples of the in situ materials may be collected and analysed, geotechnical field tests, such as the standard penetration test (SPT), which can be correlated with other engineering parameters, the use of modern geophysical techniques for mapping structures of the subsurface and geologic field reconnaissance, including the examination of in situ materials, man-made structures and groundwater level (Soupios et al., 2007). Among these, geophysical methods with continuous measurement can provide copious information over a wide range of area. Borehole provides information from only its location invading the formations but does not show the extent. Generally, collecting data without invading or non destructively from a

prefered area is a major concern in any geophysical exploration (Olona et al., 2010a; Scollar et al., 1990).

Over the past three decades in West Africa and Ghana to be precise, the application of geophysical techniques in site investigations for civil engineering works is gradually gaining roots. Application of geophysical methods in geotechnical investigations has the capability of bringing out the subsurface image of a construction site which is very essential to the civil engineer (Goldstein, 2009; Benson et al., 1984; Benson and Yuhr, 1995; 2002). It must be admitted as a fact, that lack of knowledge about the subsurface strength distribution at a site before erecting a structure is in disguise a risk to the inhabitants and people living in its environment. Normaly, questions pertaining to the foundation of buildings come to the fore when issues of buildings submerging under their load arise at a later time. Early detection of subsurface conditions that may pose potential danger to a building is crucial at the begining and can be accomplished with geophysical survey. Undetected cavities, fissures and other near surface features such as high clay content are the sources and risk to buildings put up without any geotechnical investigations.

Unfortunately, a lot of buildings are constructed on soils with insufficient bearing capability to support the weight of the structure. These soils may be partly made of expansive clays that shrink or enlarge as the moisture content is changed and can cause the foundation of these buildings to respond resulting in unexpected breakdown from cracks if the moistening and drying of the clay is anomalous. Geological features and conditions beneath the surface such as voids, conduits, fractures, nearness of the water table to the surface, depth to bedrock are some of the prominent threats to the foundations of buildings (Andrews et al., 2013; Cecil, 1971).

Electrical resistivity tomography (ERT), high resolution seismic, magnetic, the ground penetrating radar (GPR) and electromagnetic (EM) methods are the most commonly employed geophysical techniques in near surface exploration for natural resources, geotechnical evaluation and environmental assessment (Butler, 2005).

Widely applied in assessing the suitability of the near subsurface conditions in sites which involve subways, tunnel alignment, nuclear power plants, bridges, roads, dams, quarries and hydroelectric power plants is the high resolution seismic refraction. Refraction seismic is one of the most effective geophysical tools that has gained much engagement in site investigation for civil engineering work. It is a simple and effective means of obtaining valuable p-wave velocity information about a large volume of the subsurface in 2D. P-wave velocity affects a number of geotechnical properties such as elastic and shear moduli, porosity and poisson ratio. In seismics, velocities sometimes may not be influenced by clay and low friction joint filling which are some of the causes of instability in a rock mass and must be taken into consideration in interpretation of refraction seismic data.

Though refraction seismic may be limited as a result of geometries of the subsurface like hidden and thin layers (lower velocity layer sandwitch in high velocity layers), refraction seismic is capable of revealing significant information about the velocities of layers beneath the surface besides their thicknesses, elastic properties and water content when used in conjunction with particularly exploratory drill. Seismic refraction data can therefore strengthen the usefulness of exploration drill data (Rucker, 2000; Dutta, 1984; Sjøgren et al., 1979; Hatherly and Neville, 1986; Kilty et al., 1986; Moustafa et al., 2012).

One leading basic application in the early days of the seismic refraction technique was to estimate the depth to bedrock but the method has been successful in the mapping of weak

shear and faulted zones and also to indicate the quality of rock mass in fresh igneous and metamorphic rocks. These faulted and shear zones are characterized by lower velocities in reference to the host rock formations. Refraction seismic technique makes effective use of the propagation of an elastic compressional (primary) seismic wave. The bulk and shear moduli of the rock can be estimated from the ratio of the longitudinal and transverse sonic velocities (Sjögren, 1984; Sjøgren et al., 1979). Anthropogenic activities (mining, burning of fossil fuels etc), excess pore water pressure besides weathering of the soil profile are some of the factors contributing to the loss in shear strength. Reduction in shear strength can lead to landslides on slopes. The seismic refraction method has been applied to study these factors that can cause landslide in addition to other geotechnical problems like compaction certification, evaluation of bearing capacity, earthquake site classification and subsidence investigation (Varnes, 1978).

Besides seismic refraction, the geoelectrical resistivity imaging technique is also increasingly becoming popular in environmental and engineering investigations (Coskun, 2012; Aizebeokhai, 2010; Yilmaz, 2011). 2D multi-electrode electrical imaging system which simultanuously takes into accounts sounding and profiling has successfully been applied to map areas with fairly complex geology (Dahlin and Loke, 1998; Griffiths and Barker, 1993; Amidu and Olayinka, 2006; Aizebeokhai et al., 2010; Olayinka and Yaramanci, 1999). Depending on how the survey is designed and carried out, the electrical resistivity tomography can be used to acquire data that will give subsurface images in either two or three dimensons. Lately because automated data acquisition systems and efficient user friendly inversion softwares are accessible, the electrical resistivity imaging technique has the potential to give more reliable images of the subsurface (Aning et al., 2013).

Electrical resistivity method has wide variety of applications with the objective to determine

the physical parameters of a rock formation and map geologic structures in mineral and groundwater exploration and also investigate the subsurface (Soupios et al., 2007; Aning et al., 2014; Lowrie, 1997; Telford and Sheriff, 1990; Andrews et al., 2013). Subsurface geology in geotechnical and environmental assessments is generally heterogeneous and multi-scale such that the physical properties vary both vertical and laterally.

In this work, the seismic refraction and resistivity methods were used to image the subsurface and find it capacity to hold the weight of giant buildings.

1.2 Review of Literature

Ambiguities in geophysical data interpretation make the demand for an integrated survey very imperative. The combined use of geoelectrical resistivity and seismic refraction techniques for site investigations these days is very effective because each method has a distinct response to a geophysical property with varying resolution. Elastic p-wave velocities and apparent resistivity values from beneath the subsoil in a given area can give comprehensive geological information and helps draw good conclusions and predict which part of the subsurface has a good load bearing capacity.

To assess the nature of the subsurface at the site for the proposed KNUST Teaching Hospital building in Kumasi-Ghana, Andrews et al. (2013) employed the 2D and 3D geoelectrical resistivity imaging technique. Their work was mainly to locate faults, voids, clay, water-table and depth to the bedrock. They used the multi-electode ABEM Terrameter SAS 4000 with the Wenner array and an electode separation of 4 m to collect 2D resistivity data over 28 profile lines each 200 m in length. The geoelectrical method used by Andrews et al. (2013)

was able to delineate potential clay portions at the site in addition to weak zones like voids that cannot support the load of the buildings and other part with leachate from a nearby old waste dump site. From their pseudosections, part of the subsurface was made of clay but no faulted zones were found.

The seismic refraction survey has been used by Palmström (1996) in a geotechnical study to assess the jointing in rock mass which gives information about the quality of the rock. Palmström found out a seismic refraction limitation in jointing assessment due to the fact that, seismic velocity is controled by many properties and features which make uncertainties inevitable when variations in the velocity is predominantly linked to one or more of these. Moreover, where the stress level is moderate or low at near surface, seismic refraction gives satisfactory results as closing of joints are due to increase in stress level which is an indication of variation in joint density.

Khan (2013) used shallow seismic refraction and electrical resistivity techniques in an integrated engineering geophysical approach to assess unconsolidated topsoil. The motive of his work was to determine the nature of the shallow subsoil with the refraction seismic and confirm it using the resistivity method. He used the SAS 4000 ABEM Terrameter with the Shlumberger array and a 24-channel Geometrics digital seismograph (Geode) for the resistivity and seismic data collection respectively. Two levels of weathering within the overburden of thickness 4 m were revealed. These layers of weathering composed of superficial dry unconsolidated sediments showing high resistivity influenced by the air spaces. This is underlain by a thicker conductive water saturated layer with clay which the resistivity method easily delineated.

Moustafa et al. (2012) in Southwest of Saudi Arabia assessed the source and groundwater

pathway seepage under a dam site by combining dc resistivity and near surface seismic refraction methods. In doing this, they used a 48-channel seismograph with a geophone separation of 5 m for refraction seismic data over three profile lines. Four layers were delineated with fractures in the third layer. These fractures have resulted in two depressions which extend in the form of buried channels filled with porous alluvium and fractured greenstone. Interconnected fractures in rocks are permeable zones and represent favourable pathway for leakage of dam water.

Geotechnical evaluation of soil at the site for the Teaching Hospital project at Mosul University in Mosul City, Iraq, has been done by (Ahmed, 2014). To determine the engineering parameters such as stress ratio, material index and density gradient, they employed a 12-channel ABEM Terraloc MK.6 seismograph and a sledge hammer as p-wave source to carry out the refraction seismic survey over twelve profile lines each of length 280 m. In this work, three acoustic layers were identified. From the elastic wave velocities that were computed, the first and second layers composed of recent superficial deposits and river terraces respectively but the third layer had high velocity and very competent for building foundation purpose. P-wave velocity gives valuable information in determining soil types and their level of weathering which affects compaction.

Seismic refraction has been used in many parts of the world to delineate aquifer zones capable of producing potable water. The groundwater level is known to be a boundary of acoustic impedance by seismic refraction method and this is of much interest to the geotechnical engineer (Ushie and Eminue, 2013). Olona et al. (2010b) successfully mapped weathering variations in a granitic massif and related geotechnical properties such as rock quality designation and weathering grade by integrating seismic refraction and electrical resistivity methods in parts of North-West Spain. At the proposed site for Kauridan Estate

at Ibagwa-Nike, Southeastern Nigerian, Ugwu and Ezema (2013) used the 2D electrical resistivity imaging technique to evaluate the subsoil. Potential subsurface structures which can pose danger to the estate houses were mapped with the multielectode ABEM Lund imaging system. 2D data have been collected on six parallel profiles using the Wenner array. Coarse sand and gravel at the near surface to a depth of about 7 m produced high resistivity values with a low resistivity underlying layer (shaley sand) with no fissures and faults zones.

A 2D electrical resistivity survey has been carried out by Osazuwa and Chii (2010) at the periphery of the reservoir of the Ahmadu Bello University farm dam in Northern Nigeria. Their work was to assess the subsurface around the dam and find out weak zones which are potential paths for seepage of dam water. 2D data was acquired on eight profiles with the ABEM Lund imaging system. There was a low resistivity zone delineated within the bedrock which represents a weak zone serving as a pathway for water from the reservoir.

1.3 Problem of The Research

Much attention has not been given to the nature of the subsoil at construction sites although there has been cases in the nation where buildings have collapse unexpectedly taking the lives of precious citizens without knowing the cause. But rather, sudden collapse of buildings have mostly been attrbuted to the use of poor building materials.

The increase in students population year after year on campus of KNUST had led to more expansion work. Over the past few years buildings such as Engineering audithorium, Chancellor's Hall, College of Science and Art buildings, the KNUST Mall at commercial area have been constructed. But the question still remains as to whethere there were any

geophysical work prior to laying the foundation of these buildings. There is the need for site characterization using geophysical methods at potential building sites on the campus for which the extension for the Business School is one.

This work aimed at using seismic refraction and electrical resistivity methods to map voids, fissures, clay, faulted zones and degree of compaction of the weathered zone at the KNUST School of Business extension site and find out its geotechnical properties.

1.4 Objectives of The Research

Geotechnical investigations are paramount for civil works such as the construction of dams, bridges and overpasses, underground tunnels, skyscrappers etc. The primary objective of the geophysicist in site characterization is to investigate the subsurface and delineate possible features that can adversely affect the foundations of structures. A fair idea of the near subsoil geologic features at a site prior to construction is essential for the civil engineer to lay the best of foundations and position a building appropriately.

Site investigations are usually carried out to determine geotechnical parameters that reflect the behaviour of the subsurface from the engineering point of view. Some parameters that are measured in geotechnical studies may include the velocity of elastic waves, soil porosity, density of rock, water saturation, shear modulus, poisson's ratio etc. All these parameters are relevant in a geotechnical work to assess a site's suitability for a particular structure. The primary role of the geophysicist in site investigation is to determine the thickness of the regolith and elastic wave velocities of acoustic layers which is a guide to the strength of rocks. Compact soils (normally volcanic soil) have low amount of pore spaces, high

bulk density and elastic wave velocity. Areas where volcanic soils predominate such as the Pacific and Caribbean islands, Central and South America, Indonesia and Africa usually fall within tropical regions with high annual rainfalls and intense precipitation most often. These volcanic soils are normally able to bear near-vertical slopes, advantage of which is often taken for road cuts (Bommer et al., 2002; Bommer and Rodriaguez, 2002).

The main objective of this research work is to examine the subsurface at the site and find out it competence for supporting structures using the seismic refraction and resistivity methods. These are the specific objectives of this research work; delineate the bedrock, examine the weathered zone and its degree of compaction and also identify voids, faults and clay zones.

1.5 Structure of Thesis

The whole body of this thesis work comprises of six chapters. Each chapter with its corresponding sections and subsections unfolds distinct information. Chapter one introduces the research problem, outlines the need for this research and also reviews work done by other people using the multielectrode dc resistivity and/or seismic refraction method.

The basic theory that underpin the electrical resistivity and the compressional p-wave refraction seismic methods are reviewed in chapter two with some data interpretation techniques.

The study area's geological settings revealing the main rock formations underlining the Kumasi metropolis is in chapter three. This chapter also unveils the location, accessibility and climatic conditions of the site, design of the survey, methods and other field procedures adopted for a successful data acquisition. Further discussed in this chapter are the processing

steps and the softwares used.

Interpretation of the 2D resistivity model section and seismic refraction velocity-depth models are presented in chapter four. Also, this chapter presents geologic implications of the results and 3D models of the top of the refracting interfaces.

Finally, chapter five draws inference from the outcome of the research and make recommendations for future work.

CHAPTER 2

BACKGROUND THEORY

2.1 The Seismic Method

2.1.1 Overview of Seismic Waves and Velocity

A single shot seismic record has direct, refracted and reflected waves. In an environment with faulted zone in the bedrock, diffracted waves are also recorded. In this work only refracted seismic waves are made use of.

Seismic waves are in the form of packets of elastic strain energy that travel from a naturally or artificially generated source. It has two major components, the Body and Surface waves (Reynolds, 2011). Body waves propagate through the whole internal structure of the earth. It comprises of the compressional (primary (P)) wave and shear (secondary (S)) wave.

P-waves are longitudinal and cause the particle of the medium to vibrate in the same direction as the wave propagate but s-waves are transverse and cause the particles of the medium to vibrate perpendicular to direction of propagation of the wave. In the same medium, p-wave travels faster than s-wave.

Surface waves are in the form of Rayleigh and Love waves. These waves travel along the surface of the Earth with a more complicated particle motion and are responsible for damages

during the release of energy from earthquakes (Kearey et al., 2009; Sheriff, 2002). The velocities with which seismic pulses move are determined by the density (ρ), the bulk (K) and shear moduli (μ) of the medium through which they pass. The seismic velocities are given by the following relations:

$$V_p = \sqrt{\frac{K + \frac{4}{3}\mu}{\rho}} \tag{2.1}$$

and

$$V_s = \sqrt{\frac{\mu}{\rho}} \tag{2.2}$$

The estimated primary wave velocity from a refraction seismic survey is linked to porosity (ϕ) of a rock with the equation below.

$$\frac{1}{V_p} = \frac{\phi}{V_f} + \frac{1-\phi}{V_m} \tag{2.3}$$

V_f is pore fluid velocity typically 1500m/s and V_m is the velocity of the rock matrix (2800 m/s) (Wyllie et al., 1958; Reynolds, 2011).

In near surface seismic exploration geophysics, elastic p-wave velocity is normally utilized but developments in recent years combine s-waves with p-waves for lithostratigraphic characterization (Telford and Sheriff, 1990).

2.1.2 Seismic Refraction Method

In a homogeneous earth layer, a wave travels in a straight path but changes direction as it enters a different acoustic layer (figure 2.1). The ratio of the sine of the incident angle to the sine of the angle of refraction is equal to the ratio of the velocity of the first layer to that of the second layer given by equation 2.4. As the incident angle increases, the refracted angle in the second layer also increases. Critical refraction is reached when the angle of refraction in the second layer equals 90^0 as the incident angle is further increased. At critical refraction, the refracted ray travels along the interface separating the two acoustic layers.

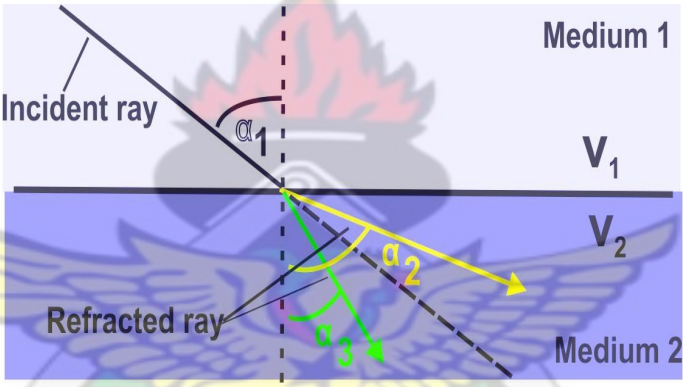

Figure 2.1: Schematic diagram of a p-wave travelling from a top layer with velocity V_1 into a layer with velocity V_2.

$$\frac{sin\alpha_1}{sin\alpha_2} = \frac{V_1}{V_2} \tag{2.4}$$

In refraction seismology, part of the seismic impulses sent into the subsurface are critically refracted in response to changes in acoustic impedance of the earth layers. Acoustic impedance is the product of the density (ρ) of a given formation and its velocity. The critically refracted waves travelling along the discontinuous boundary break off to the surface as head waves (figure 2.2) as points on the wavefront act as secondary wave sources based

on the Huygens' principle. Equation 2.5 and 2.6 give the relationship between the critical angle (i_c), refracted angle (90^0) and the layer velocities (V_1 and V_2).

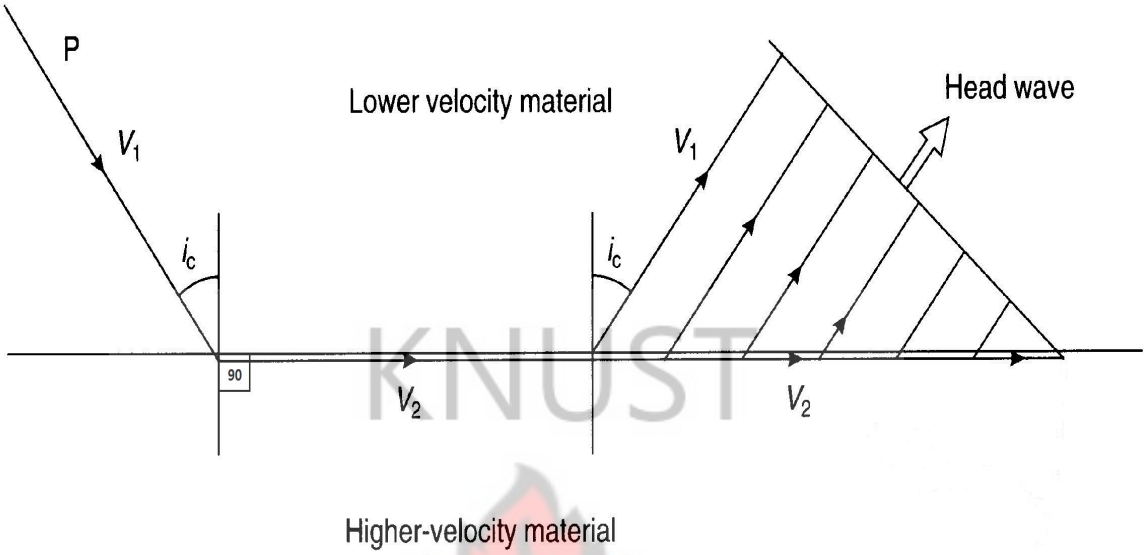

Figure 2.2: Schematic diagram showing critically refracted p-wave at a plane boundary generating upward moving header waves. V_1 and V_2 are the velocities of the overburden and underlying layers respectively and i_c the critical angle (Telford and Sheriff, 1990).

$$\frac{sini_c}{sin90^0} = \frac{V_1}{V_2} \tag{2.5}$$

$$sini_c = \frac{V_1}{V_2} \tag{2.6}$$

2.1.3 Traveltime Curve, Velocity and Layer Thickness

The time taken for seismic pulse to arrive at the receivers (geophones) are plotted against the distance of the receivers from the shot location in order to compute the velocities of layers present using the slopes of the T-X curves (figure 2.3). The direct wave plot passes through the origin and has velocity V_1 given by the inverse of its slope (equation 2.7). The distance

from the shot location to the point the refracted waves start arriving at the geophones is the critical distance (X_{crit}). From the crossover point (X_{cross}), the refracted waves take over as first arrivals. Velocity of the refracted waves (V_2) is given by equation 2.8.

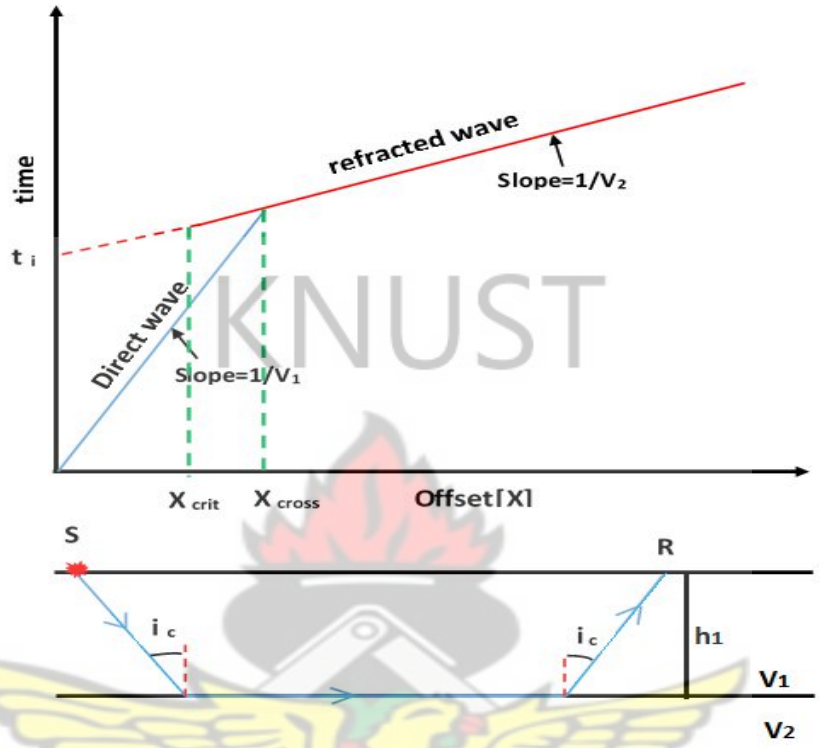

Figure 2.3: A traveltime curve of seismic refraction first arivals. V_1 and V_2 are velocities of the first and second layers respectively. Note : V_2 is assumed to be greater than V_1.

The layer velocity is related to the slopes of the travel time plot according to the following equations:

$$slope\_{direct} = \frac{1}{V_1} \tag{2.7}$$

$$slope\_{refracted} = \frac{1}{V_2} \tag{2.8}$$

The velocities obtained from the slopes of the traveltime curve are used to find the layer thicknesses. Refraction seismology uses velocity and layer thickness to describe the subsurface geology. The arrival time t_x of a pulse at the receiver placed at a distance X

from the shot point is given by equations 2.9 and 2.10.

$$t_x = \frac{X}{V_2} + \frac{2h_1\sqrt{V_2^2 - V_1^2}}{V_1 V_2} \tag{2.9}$$

$$t_x = \frac{X}{V_2} + t_i \tag{2.10}$$

t_i is intercept time and h_1 the depth to the refracting interface. If the shot and receiver locations are assumed to be at the same point, then X = 0 and $t_x = t_i$. The following equations therefore holds for t_i and h_1 (thus the depth to the first refracting interface).

$$t_i = \frac{2h_1\sqrt{V_2^2 - V_1^2}}{V_1 V_2} \tag{2.11}$$

$$h_1 = \frac{t_i V_1 V_2}{2\sqrt{V_2^2 - V_1^2}} \tag{2.12}$$

2.1.4 Multiple Layer

For a subsurface with multiple acoustic horizontal layers (Figure 2.4), the principle of reciprocity is valid. Both the forward and reverse traveltime curves are of the same nature with a symmetrical crossing point of the refraction curves about the profile. The arithmetic mean of the apparent velocities obtained from the refraction curves is equal to the true velocity of the refractor. Generally, the travel time equation for a subsurface with many horizontal plane layer interfaces is given by equation 2.13. Where ”n” is the number of layers and ”i” is the refracting interface number.

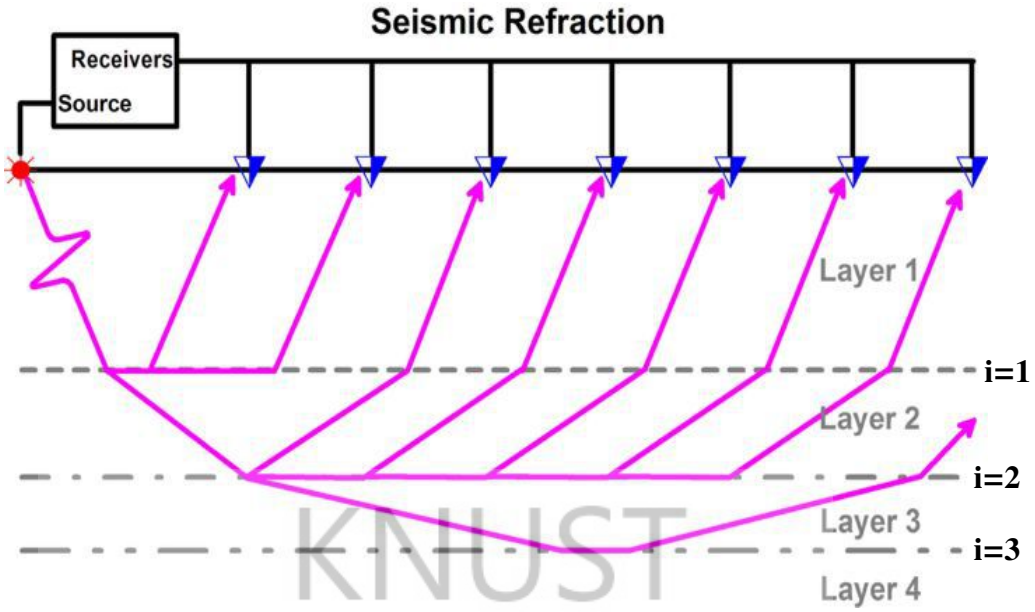

Figure 2.4: Refraction at multiple horizontal interfaces (Downloaded from www.google.com/seismic refraction/images on the 24th July, 2014)

$$t_x = \frac{X}{V_n} + \sum_{i=1}^{n-1} \frac{2 * h_i \sqrt{V_{i+1}^2 - V_i^2}}{V_{i+1} * V_i} \tag{2.13}$$

2.1.5 Dipping Layers

Traveltime curve for a nonparallel or dipping refractor gives apparent velocity which can result in incorrect depth computation. The crossing point [CP] of the forward and reverse refraction curves is nonsymmetrical about the profile. It always shift towards the down-dip direction. Interchanging the shot and receiver positions would not produce the same travel-time curves (figure 2.5).

$$V_{2U} = \frac{V_1}{sin(i_c - \gamma)} \tag{2.14}$$

$$V_{2D} = \frac{V_1}{sin(i_c + \gamma)} \tag{2.15}$$

The dip angle (γ) is related to the velocity of the first layer (V_1), refractor's velocity in up-dip direction (V_{2U}) and that in the down-dip direction (V_{2D}) by equation 2.16.

$$\gamma = \frac{1}{2}[sin^{-1}(\frac{V_1}{V_{2D}}) - sin^{-1}(\frac{V_1}{V_{2U}})] \tag{2.16}$$

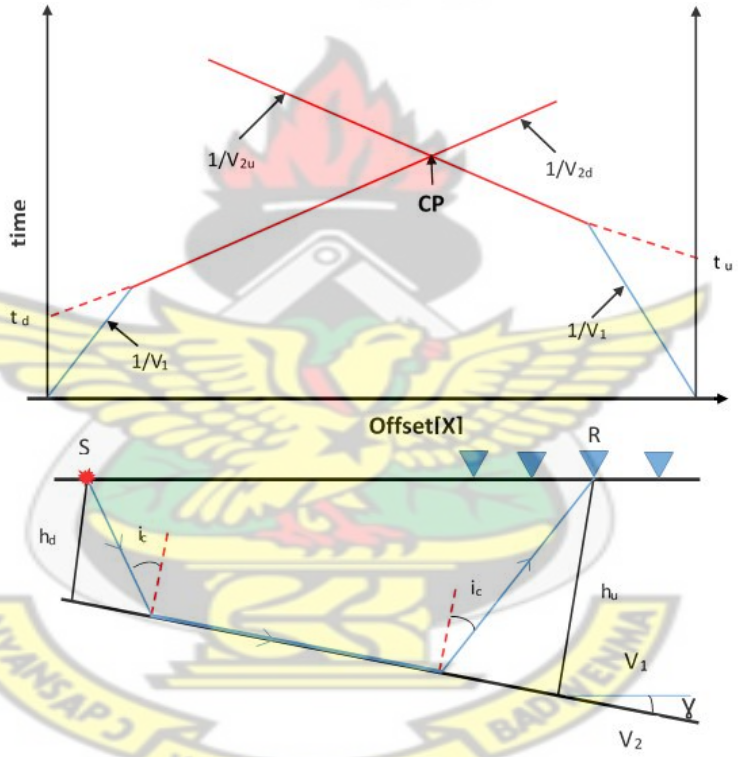

Figure 2.5: Schematic diagram of a dipping interface. t_d is the down-dip intercept time, t_u is up-dp intercept time, V_{2d} and V_{2u} are the velocities of the refractor in the down and up-dip directions respectively and CP is the crossing point of the refracted traveltime curves.

The critical angle is given by:

$$i_c = \frac{1}{2}[sin^{-1}(\frac{V_1}{V_{2D}}) + sin^{-1}(\frac{V_1}{V_{2U}})] \tag{2.17}$$

Velocity in the up-dip shot is always greater than that in the down-dip. The extent of dip of the refractor determines the magnitude of its apparent velocity.

$V_{app} = V_{true} : \gamma = 0^0$.

$V_{app} = \infty : \gamma = 90^0$.

The true velocity of the half-space is given by the product of the cosine of the dip angle and the harmonic mean but not the arithmetic mean of the measured up and down dip velocities (equation 2.18). This velocity of the seismic waves predicts the kind of material present in the propagating medium (table 2.1) with the aid of geologic information of the area.

$$V_2 = \frac{2V_{2U}V_{2D}}{V_{2U} + V_{2D}} cos\gamma \tag{2.18}$$

Depth to the refractor in the down-dip (h_d) and up-dip (h_u) directions are given by:

$$h_d = \frac{V_1 t_d}{2cosi_c} \tag{2.19}$$

$$h_u = \frac{V_1 t_u}{2cosi_c} \tag{2.20}$$

Table 2.1: A table of elastic wave velocity for some earth materials in ice (Kohnen,1974). Depend strongly on tempareture.

Material	**V_p(m/s)**
Air	330
Water	1450-1530
Sand(Loose)	200-2000
Sand(Loose, dry)	200-1000
Sand(Water saturated, loose)	1500-2000
Floodplain alluvium	1800-2200
Sandstone	1400-4500
Limestone	1700-4200
Dolomite	2500-6500
Shale	2000-4500
Rock salt	4000-5500
Granites	4600-6200
Gabbro	6400-7000
Basalts	5500-6500
Gneiss	3500-7600

2.2 The Geo-electrical Resistivity Method

Induced polarization, self-potential and resistivity are among the electrical survey methods. Electrical methods use direct currents (dc) or low frequency alternating currents to investigate the electrical properties of the subsurface. The induced polarization method makes use of the capacitive action of the subsurface to locate zones where conductive minerals are disseminated within their host rocks. Self-potential method makes use of natural currents flowing in the ground that are generated by electrochemical processes to locate shallow bodies of anomalous conductivity. The resistivity method uses current injected into the subsurface to study horizontal and vertical discontinuities in the electrical properties of the ground. Electrical surveys in which currents are made to flow inductively are referred to as electromagnetic (EM) surveys (Kearey et al., 2009).

Electric current has three ways of conducting through rocks namely dielectric, electronic (Ohmic) and electrolytic. Electrolytic conduction occurs by the relatively slow movement of ions within an electrolyte in a rock matrix. Electronic conduction involves rapid movement of electrons in metals. Dielectric conduction occurs in very poor conducting materials (or insulators) when an external alternating current is applied, so causing electrons to be shifted slightly with respect to their nuclei. In most rocks, conduction is electrolytic as a result of fluids in their pores (Milsom, 2007; Kearey et al., 2009).

2.2.1 Current flow in a continuous medium

Considering an element of a homogeneous material in figure 2.6 with length L and crossectional area A, there is a potential drop between the ends of the material when current I is passed through as a result of the resistance (R) by the medium. Ohm's law links the current (I), potential difference (V) and resistance (R) according to equation 2.21.

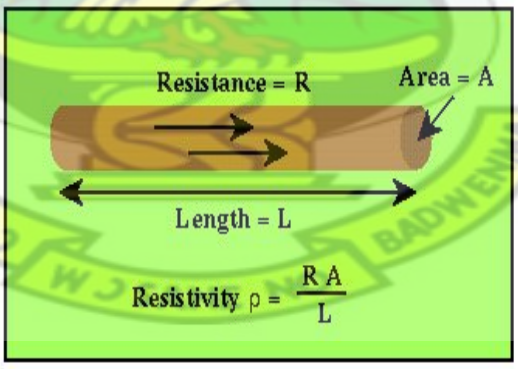

Figure 2.6: Schematic diagram of a current carring conductor.

$$V = R * I \tag{2.21}$$

$$R = \frac{\rho L}{A} \tag{2.22}$$

The resistance of the medium is given by equation 2.22 where "ρ" is the "true resistivity" which is the property of the isotropic conducting medium that opposes the current flow. For an anisotropic medium, resistivity varies and the output resistivity is not the true value of the medium but "apparent resistivity (ρ_a)".

A single electrode on a surface with a uniform subsurface of resistivity (ρ) (figure 2.7) requires a current sink at a large distance from the electrode to complete the circuit. Current flows radially away from the electrode so that the current distribution is uniform over hemispherical shells centred on the source electrode (Kearey et al., 2009). A shell at any point "r" in the medium from the electrode has a surface area (A) of $2\pi r^2$. The current density (J) and potential gradient ($\frac{\partial V}{\partial r}$) are respectively given by equations 2.23 and 2.28.

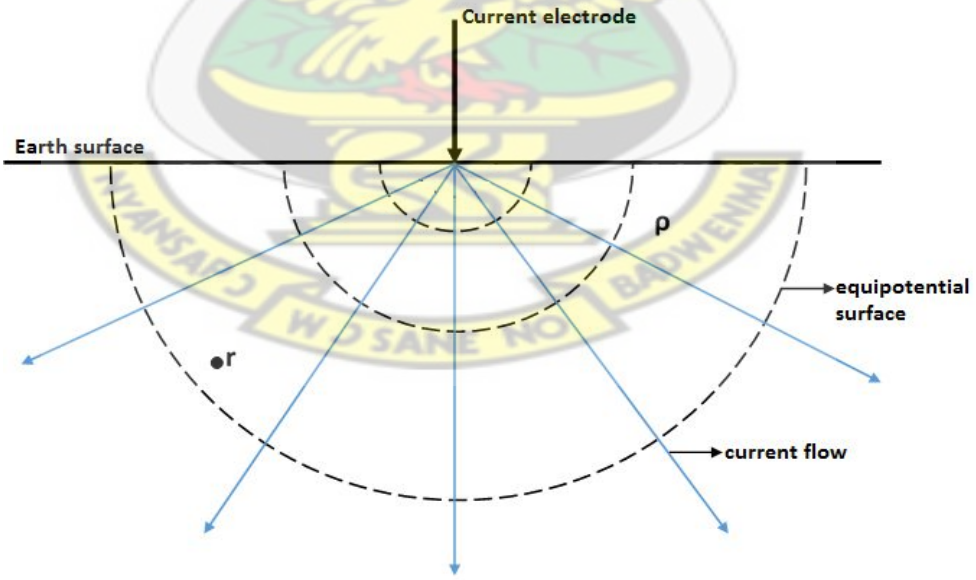

Figure 2.7: Current flow from an electrode through an isotropic subsurface.

$$J = \frac{I}{A} = \frac{I}{2\pi r^2} \tag{2.23}$$

Also

$$J = \sigma E \tag{2.24}$$

but

$$E = -\frac{\partial V}{\partial r} \tag{2.25}$$

and

$$\sigma = \frac{1}{\rho} \tag{2.26}$$

therefore

$$J = \frac{1}{\rho}(-\frac{\partial V}{\partial r}) \tag{2.27}$$

hence

$$\frac{\partial V}{\partial r} = -\rho J = -\frac{\rho I}{2\pi r^2} \tag{2.28}$$

The potential (V) measured at any point ”r” in the homogeneous subsurface is the integral of

the potential gradient given by equation 2.30.

$$V = -\frac{\rho I}{2\pi}\int \frac{1}{r^2}\partial r \tag{2.29}$$

$$V_r = \frac{\rho I}{2\pi r} \tag{2.30}$$

Electrical resistivity surveys are carried out with the conventional four electrode or continuous vertical electrical sounding (CVES)/multi-electrode system. In either case, an artificially generated electric current is injected into the ground through two current electrodes and the resulting potential at point in the subsurface measured with two potential electrodes to compute the resistivity.

2.2.2 The Four Electrode System

The four electrode system uses two current and two potential electrodes for the survey. The current is sent into the ground through the electrodes A and B and the potential at any two points on the surface measured with electrodes M and N (Figure 2.8).

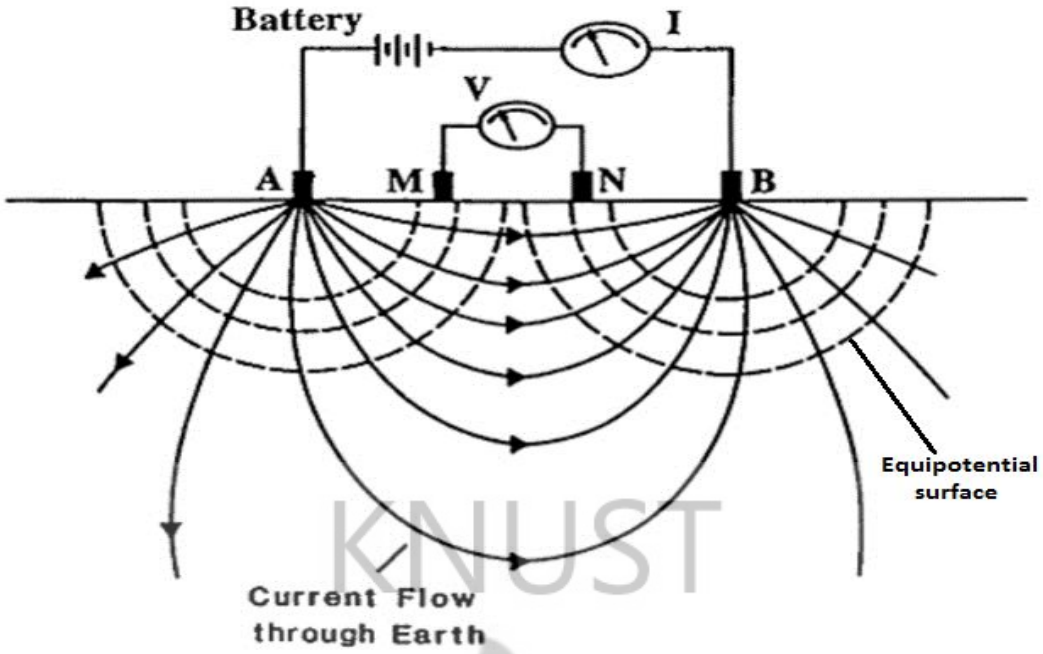

Figure 2.8: A diagram of the conventional four electrodes showing current flow pattern and the equipotential surface. A and B are current electrodes with M and N as potential electrodes.

Given the geometric factor k (equation 2.31) which is strictly determined by the arrangement of the electrodes, the apparent resistivity is given by equation 2.32.

$$k = \frac{2\pi}{[\frac{1}{AM} - \frac{1}{MB}] - [\frac{1}{AN} - \frac{1}{NB}]} \tag{2.31}$$

$$\rho_a = \frac{\Delta V}{I} k \tag{2.32}$$

2.2.3 Array Types

There are different configurations of the electrodes used in electrical resistivity survey. The choice of an array in a particular work may depend on the anticipated depth of probe and

other objectives of the survey, such as mapping of dykes, sills etc. Diagrams of some electrode arrangements known in resistivity survey are shown in figures 2.9-2.15.

Wenner Array

This array has a pair of potential electrodes between two current electrodes (figure 2.9) in a straight line. The electrodes have equal separations (a). The wenner array has better sensitivity to vertical changes in apparent resistivity beneath the array's midpoint (Loke, 2001). This electrode cofiguration is good for resolving horizontal structures (eg. sills). The apparent resistivity as a result of the wenner configuration is given by equation 2.33.

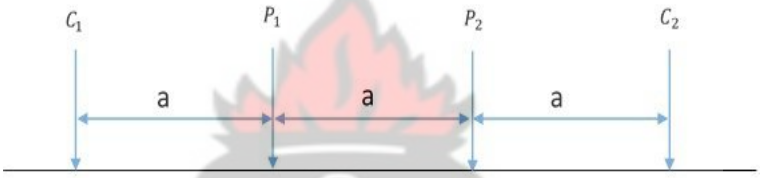

Figure 2.9: An electrode configuration of the Wenner array.

$$\rho_a = 2\pi a \frac{V}{I} \tag{2.33}$$

Dipole-dipole Array

This arrangement has two equally spaced current and potential electrode pairs (figure 2.10). The two pairs of electrodes are separated by a distance "an". The factor 'n' is the ratio of the distance between C_1-P_1 electrodes to the C_2-C_1/P_2-P_1 separation (a) and should not exceed 6 in a survey as resolution becomes very poor beyond this value (Loke, 2001). Hence "a" should be increased when "n" is approaching 6. The sensitivity of the dipole-dipole array concentrates below either the current electrode pair or that of the potential. Generally it is sensitive to horizontal changes in resistivity and can easily detect vertical structures (conduits, dykes etc.). This array is very popular in induced polarization (IP) work. Equation

2.29 gives the apparent resistivity as a result of the dipole-dipole arrangement.

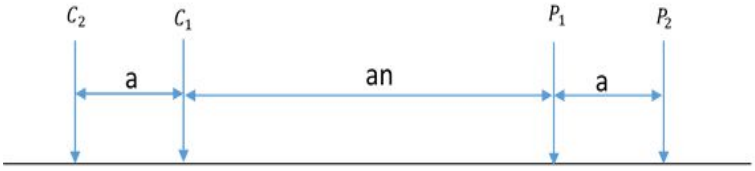

Figure 2.10: The dipole-dipole configuration.

$$\rho_a = \frac{V}{I}\pi an(n+1)(n+2) \tag{2.34}$$

Pole-dipole Array

This array also has two pairs of current and potential electrodes separated by "an". Here the second current electrode is placed at a far end (figure 2.11). Pole-dipole array is a good detector of vertical structures as it has good horizontal coverage (Loke, 2001). It is less prone to telluric current and has a better signal strength. Equation 2.35 gives the apparent using the pole-dipole array.

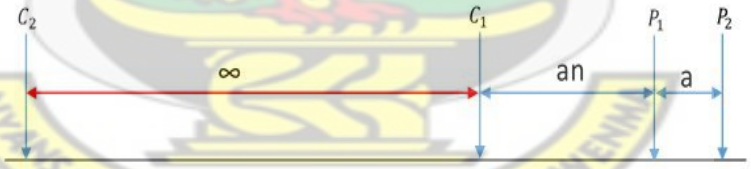

Figure 2.11: A pole-dipole configuration with C_2 as the remote current electrode.

$$\rho_a = 2\pi an(n+1)\frac{V}{I} \tag{2.35}$$

Pole-pole Array

As shown in figure 2.12, the pole-pole configuration has two pairs of potential and current electrodes separated by a distance "a". The second current and potential electrodes are

placed at far ends. This array is not commonly used but is well known in 3D surveys and where small electrode spacings are required such as archaeological survey. Among the other configurations, it has the poorest resolution picking up a lot of telluric noise but with the deepest depth of probe (Loke, 2001). Equation 2.36 is the apparent resistivity as a result of using the pole-pole configuration.

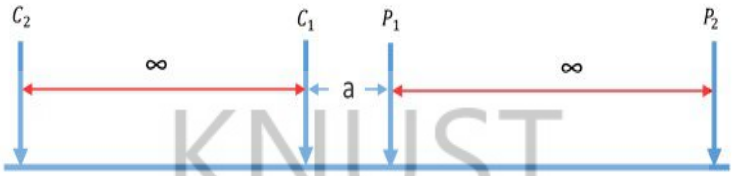

Figure 2.12: A pole-pole array showing the two remote electrodes C_2 and P_2.

$$\rho_a = 2\pi a \frac{V}{I} \tag{2.36}$$

Schlumberger Array

This electrode arrangement has a pair of potential electrodes between two current electrodes (figure 2.13). The distance between the midpoint of the potential electrodes to the first current electrode is equal to that between the second current electrode and the midpoint of the potentials. This makes the Schlumberger array symmetrical. It has a horizontal sensitivity to resistivity for low values of "n" and a vertical sensitivity when "n" values are high (Loke, 2001). "n" is the ratio of the distance between either C_1-P_1 or P_2-C_2 and the P_1-P_2 elctrode separation. Here the apparent resistivity is given by equation 2.37.

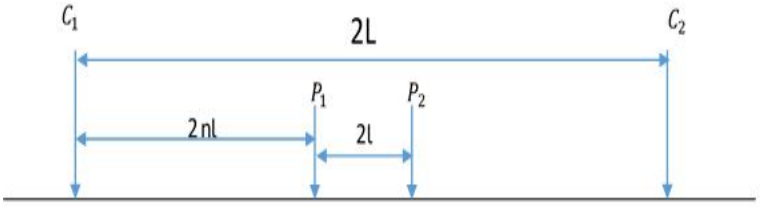

Figure 2.13: Schematic diagram of the symmetrical Schlumberger array.

$$\rho_a = \pi \frac{L^2}{2l} \frac{V}{I} \tag{2.37}$$

Gradient Array (Asymmetrical Schlumberger)

This is a Schlumberger array which is not symmetrical about its midpoint. The configuration (figure 2.14) is capable of taking large number of readings. It is normally used in reconnaissance survey. Using the gradient array, the apparent resistivity is given by equation 2.38.

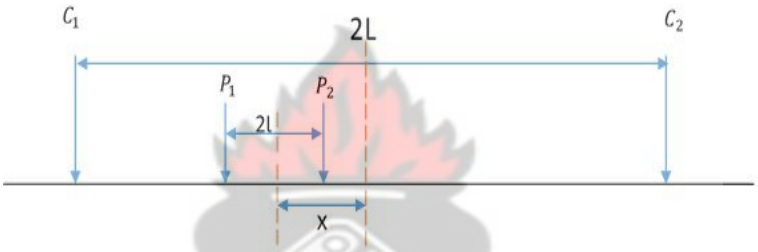

Figure 2.14: A diagram of the schlumberger asymmetrical array. "x" is the distance between the midpoints of P_1-P_2 and C_1-C_2.

$$\rho_a = \frac{\pi}{2l} \frac{(L^2 - x^2)^2}{(L^2 + x^2)} \frac{V}{I} \tag{2.38}$$

Square Array

The square configuration consist of two pairs of current and potential electrodes laid parallel (figure 2.15 [A] and [B]) or diagonal (figure 2.15 [C]). In any of these cases, the separations between the electrodes are the same, that is the side of the square (a). The electrodes are expanded symmetrically about the center during measurements, usually in increments of a $\sqrt{2}$ and has no geometric factor when used diagonally. Square array is usually used for taking data in three-dimenson and provides a measure of resistivity less orientation-dependent than that given by an in-line array such as wenner, dipole-dipole,

gradient etc (Habberjam and Watkins, 1967). 3D data taken with the square array are orientationally stable, therefore there is no need for prior knowledge of the electrical heterogeneity orientation (Senos, 2002). The apparent resistivity here is given by equation 2.39.

[A] [B] [C]

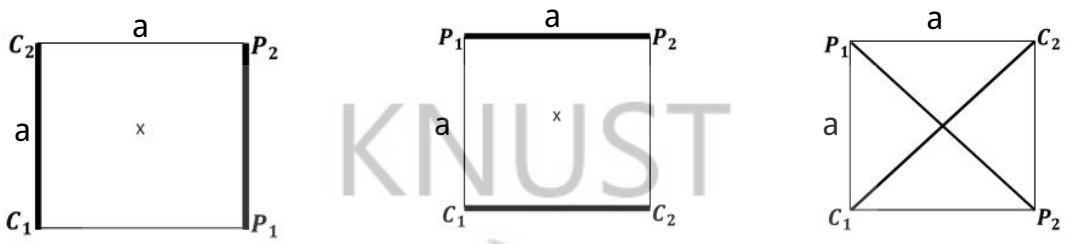

Figure 2.15: The alpha [A], beta [B] and gamma [C] square array configurations.

$$\rho_a = \frac{2\pi a}{(2-\sqrt{2})}\frac{V}{I} \tag{2.39}$$

Milsom (2007), Loke (2001) and Reynolds (2011) teach more on the different electrode configurations and their respective resolutions.

2.2.4 1D Resistivity Methods

Electrical resistivity method has two main types of measurement procedures in 1D with only four electrodes using any of the configurations discussed in subsection 2.2.4 above. These are profiling/constant separation traversing (CST) and vertical electrical sounding (VES).

In profiling (figure 2.16), the whole set of the electrode configuration is moved along the profile line at regular intervals without any change in the electrode spacing. Profilling resolves vertical structures such as dykes and shear zones (Kearey et al., 2009).

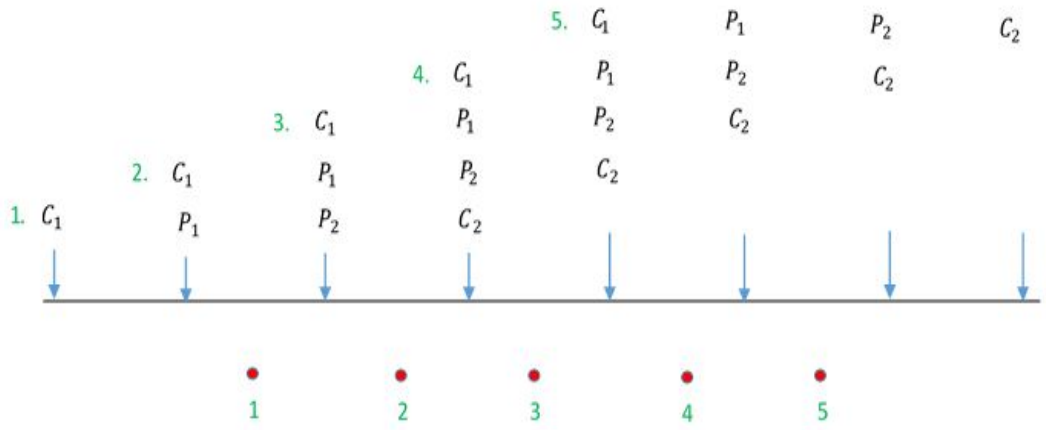

Figure 2.16: Profilling method showing the movement of electrodes using the Wenner array.

In VES, resistivity measurements are taken vertically by varying the electrode spacing about a fixed central point (figure 2.17). The 1D sounding resolves horizontal structures and good for mapping overburden thickness and delineating aquifers in bedrocks with complex geology (Kearey et al., 2009).

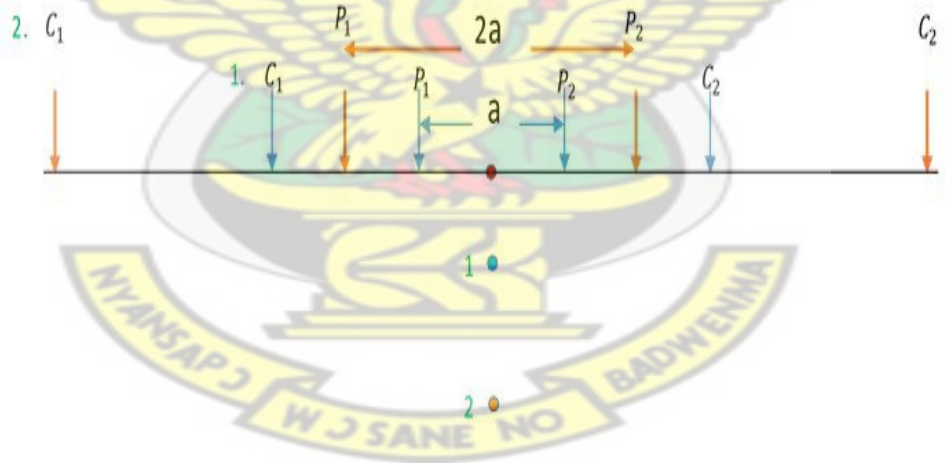

Figure 2.17: Sounding resistivity measurements using Wenner array. The electrode spacings are increased about the midpoint.

2.2.5 The Multi-Electrode System

The multi-electrode system also known as the electrical resistivity tomography (ERT) or continuous vertical electrical sounding (CVES) is a 2D method that combines profiling and

sounding at the same time in measuring the subsurface distribution of apparent resistivity. In this method, more than four equally spaced electrodes are layed on the profile line. The resistivity meter chooses a suitable electrode permutation at a time for measurements based on the selected configuration. This is repeated by the device untill there is no permutation. The resulting apparent resistivity plots take the shape of a trapezium showing the covered part of the subsurface. Reference to Loke (2001) gives more information on the electrical resistivity method using multi-electrode. Figure 2.17 demonstrates the multi-electrode configuration using the Wenner array.

The data points 1-17 in figure 2.18 use a permutation such that the electrode separation is "a". The separation is then increased to twice the initial (a) for the next readings, thus "2a" for data points 18-31. This value keeps increasing till a value for the factor "n" where no four electrodes on the profile can be used for the separation "na". Knowing the geologic setting of the area, the apparent resistivities computed can predict the kind of formations present in the subsurface (table 2.2).

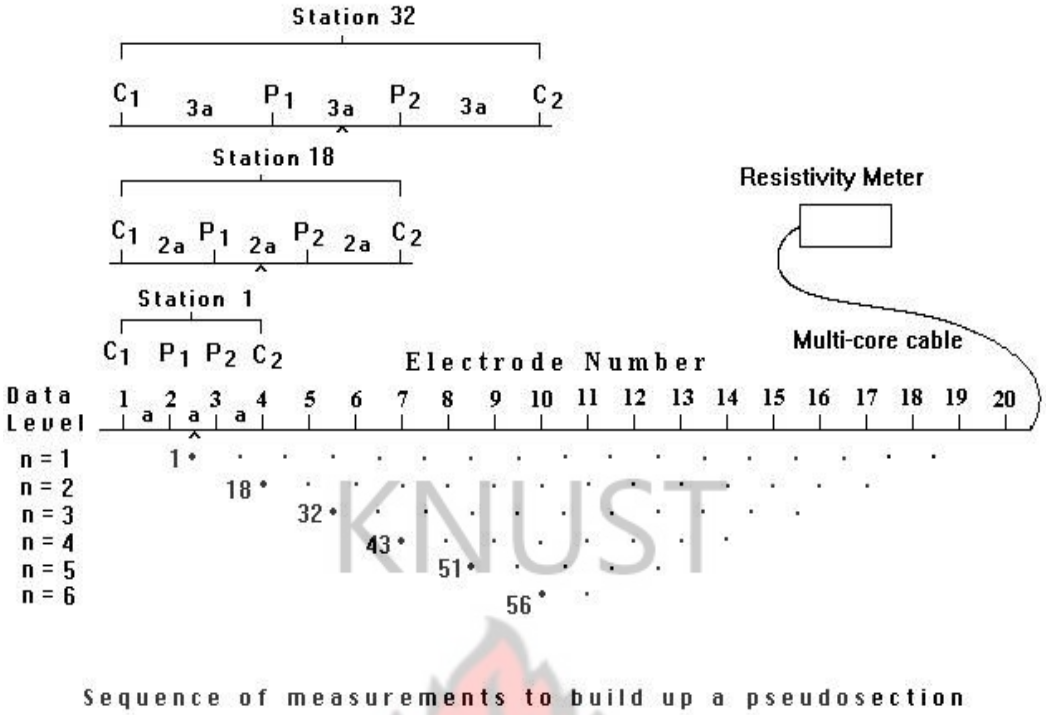

Figure 2.18: A 2D pseudosection from a multi-electrode resistivity survey using twenty electrodes (Loke, 2001).

Table 2.2: Some Earth materials and their corresponding apparent resistivity values (Loke, 2001).

Materials	**Resistivity**(Ω.m)
Granite	$6x10^3$-10^6
Basalt	$1x10^3$-10^7
Gabbro	$1x10^3$-10^6
Schist	$3x10^1$-10^4
Quarzite	$1x10^1$-10^8
Conglomerate	$3x10^3$-10^4
Sandstone	$1x10^1$-10^4
Shale	$2x10^1$-10^3
Limestone	$7x10^1$-10^3
Clay	1.0-100
Alluvium	$1x10^1$-10^3
Fresh groundwater	$1x10^1$-10^2
Sea water	0.2
Oil sands	7-900

CHAPTER 3

METHODOLOGY

3.1 Introduction

This chapter of the thesis work describes the research area, materials and geophysical methods together with the field procedures that were used for the collection of data. Besides, the various editing and processing techniques used for both the refraction seismic and dc resistivity methods are also presented in this chapter.

3.2 Location and Accessibility of Site

Kwame Nkrumah University of Science and Technology located within the Kumasi metropolis at the heart of the Ashanti region centered in the middle belt of Ghana. It falls within the transitional forest zone with varying elevation ranging between 200-271 meters ASL. The highest elevation point on the campus is recorded at the Chancellor's Hall (271 m ASL).

KNUST has vast land which covers about 18,000 m^2 with some parts undeveloped. The school has one major entry with other supporting ones linking it to neighbouring towns like Bomso, Ayeduase and Ahinsan. A feeder road runs north through south at the eastern part

of the project site to another neighbouring town, Gyinyase. KNUST has six Colleges and six traditional halls of residence with some hostel facilities in and around the campus. Its population is about 32,000 comprising of both post and undergraduate students. Farmers and traders dominate its surrounding towns. There are numerous second class roads that connects the colleges, departments, halls and other facilities on the campus (www.knust.edu.gh, 3rd March, 2014).

From the geographic point of view, KNUST is located on the following longitudes and latitudes with reference to the World Geographic System (WGS) 84 with units in decimal degree: -1.590 and 6.672, -1.564 and 6.678, -1.543 and 6.680, -1.548 and 6.693, -1.564 and 6.662 forming five of its corners (figure 3.1).

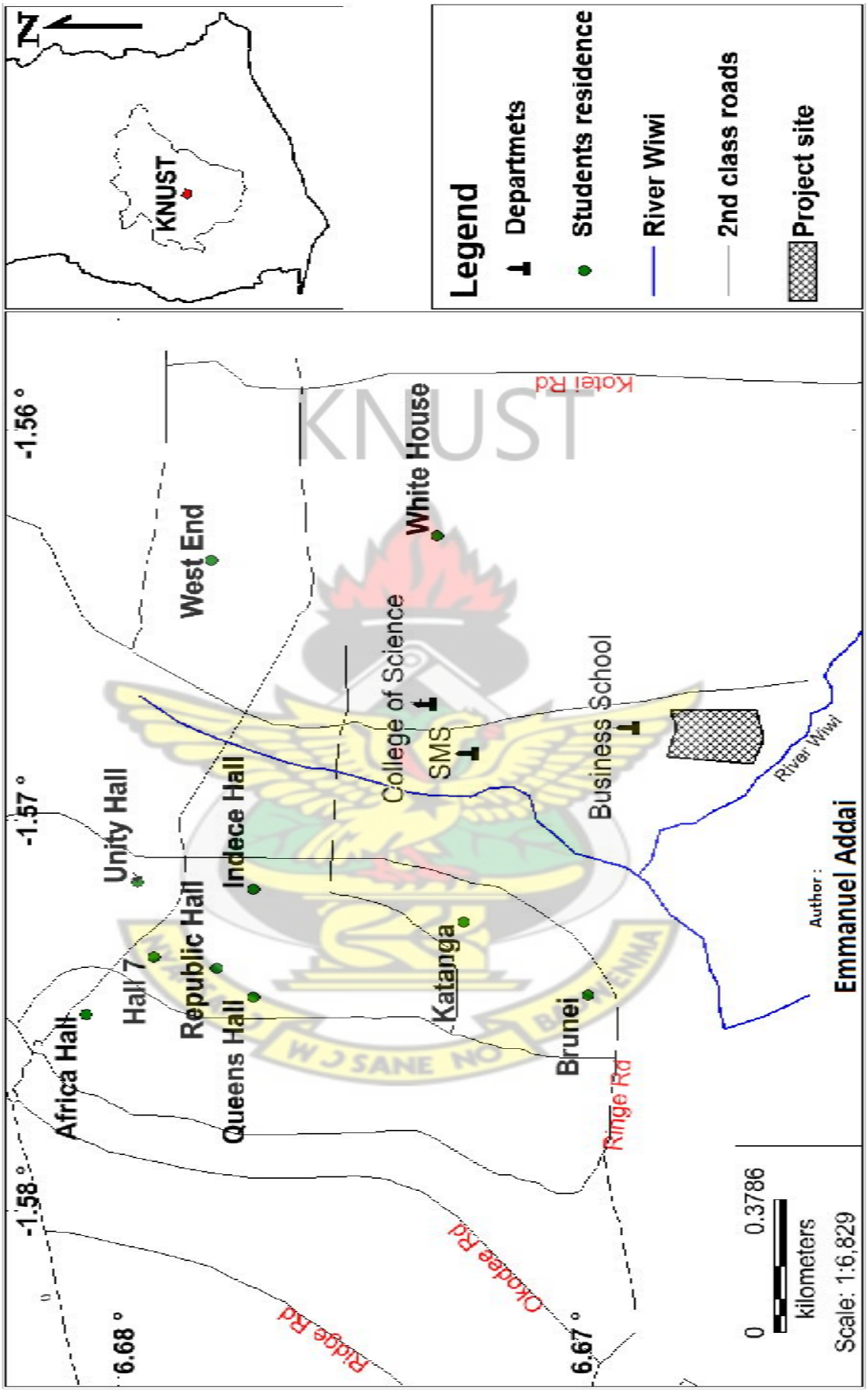

Figure 3.1: Map of KNUST showing project site. Downloaded and modified after www.knust.edu.gh (2014) on 3rd April.

3.3 Description of Study Area

The project site is a farm land covered with secondary degenerated forest vegetation on the northern and eatern sides (figure 3.2). The land surface slopes gently from north to south. Most part of the south, west and northwestern sections have grass with a river running from west through the south. Although the topsoil at the west and part of the south is mainly loose sand with low water holding capacity, it is used by the natives of neighbouring towns for vegetable cultivation. A sandy-loam soil dominates all parts of the north and east at the top.

Figure 3.2: Pictures of project site.

3.4 Physiography and Geology of Study Area

The geological setting and subsurface conditions are of much interest to any geotechnical engineer and are therefore not underestimated in this research. With a knowledge of all these, the civil engineer can then make a more reliable decision with regards to the foundation of a structure.

The rock formations that underlain most parts of Ghana which is found within the West African Craton are metamorphosed and paleoproterozoic (2300-1900 Ma) in age related to the Eburnean orogenic cycle. These paleoproterozoic rocks comprise of the Birimian and Tarkwaian groups associated with some mafic and granitoid intrusives. The Birimian supergroup is subdivided into the Lower Birimian series dominated by sedimentary units believed to be classical miogeosynclinal basin sediments. The Upper Birimian series is largely metavolcanic which represent eugeosynclinal units (Junner, 1940). Within the Birimian groups are extensive faults and folds. The Takwaian formation is on top of the Birimian and is widely exposed in the Ashanti belt (Robert et al., 2002).

The lower Birimian system is the rock formation underlying Kumasi (figure 3.3). This is compose mainly of schist, phyllites and greywackes intruded by quartz veins and stringers (GSD, 2009). Besides these intrusives is a post-Birimian Precambrian age massive granitic batholiths (Kesse, 1985) cut by pegmatite veins. Chemical weathering of the granitic bedrock and schist have resulted in dominant loose sand at the site.

The topography of the Kumasi Metropolis is that of varying elevations. It lies within the plateau of the South-West physical region which ranges from 250-300 metres above sea level.

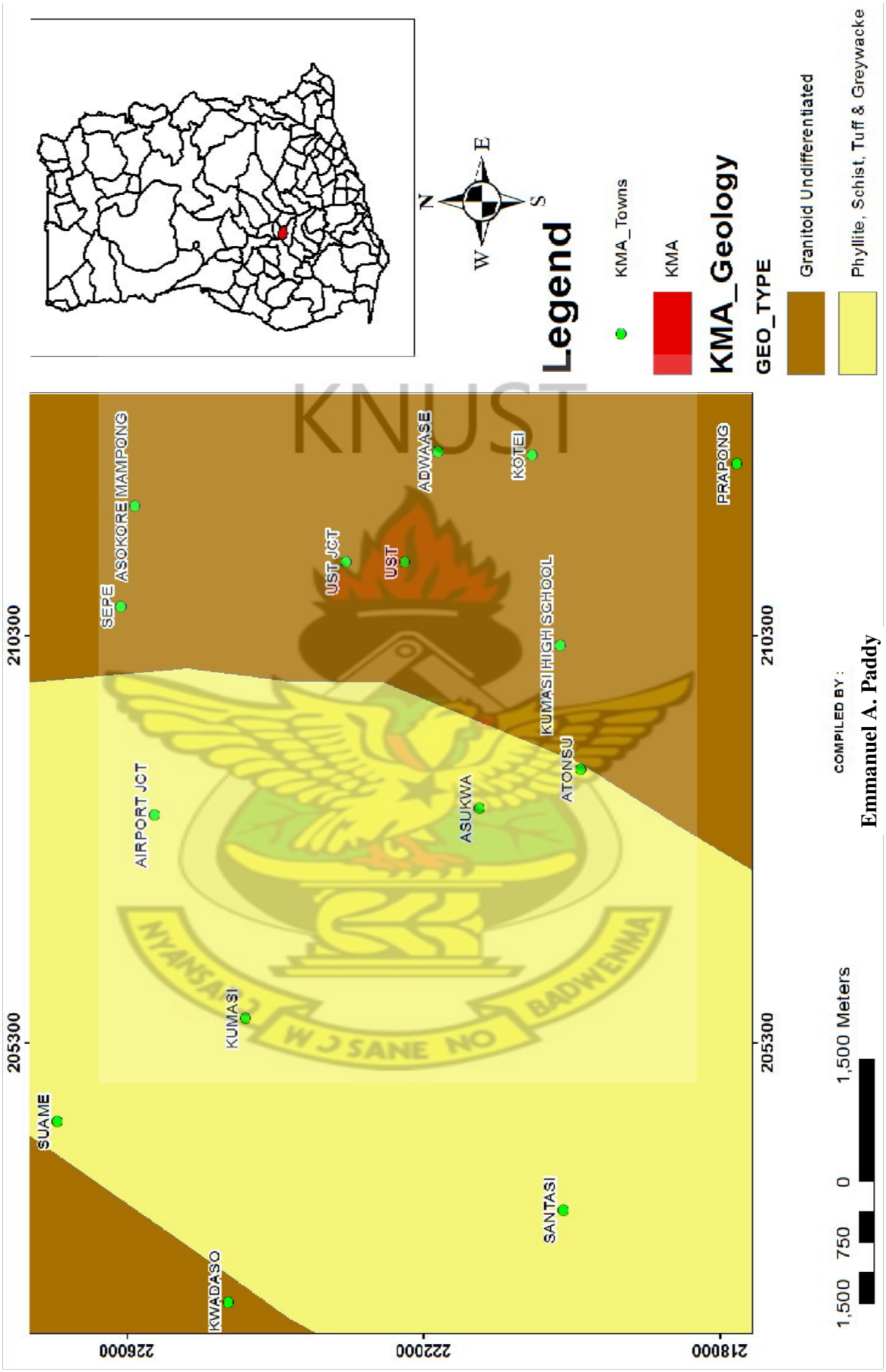

Figure 3.3: Geological map of study area. (Modified after GSD (2009)).

3.5 Climatic Conditions

According to the Köppen-Geiger classification, Kumasi has a tropical wet and dry/savanna climate with a pronounced dry season in the low-sun months, no cold season. The movement of the Inter-tropical Convergence Zone (ITCZ) influences the two seasons (dry and wet) of Kumasi.

In the dry season which normally occurs between the months of December and February, when the ITCZ has shifted southwards, dust-laden North Easterly (NE) Trade winds blows southwards over Kumasi, thereby influencing a dry period. The rainy season starts in March peaking in May with a slight drop in July. It then picks up again in August ending in November. In this season, when the ITCZ has moved northwards, moist South Westerly (SW) monsoon winds move northwards over Kumasi, thereby influencing a wet period. Temperatures for the dry season are approximately 20.4 ^{0}C minimum and 33.5 ^{0}C maximum, whereas temperatures for the wet season are approximately 21.0 ^{0}C minimum and 32.3 ^{0}C maximum respectively (www.goggle.com/ghana/districts/kma, 2014).

Kumasi has an average maximum rainfall of 214.3 mm in June and 165.2 mm in September. The minimum rainfall for Kumasi metropolis of approximately 15 mm is recorded in January. The metropolis is drained by major river bodies that traverses the city like Subin, Aboabo, Sisai, Owabi and Wiwi which passes through central part of KNUST.

3.6 Field Procedures

3.6.1 Introduction

In this part, the thesis work outlines all the activities that were carried out on the field during the collection of data. Field work started in the last week of December 2013 and ended on 28th February 2014 which fall within the dry season of Ghana where the weather is dry, hot and dusty. This was approximately for two months one week period including a try work and also cutting of profile lines. Daily transportion of equipment to the project site was made easy with a second class road linking the Physics department and Business School. The resistivity data collection took a month experiencing some breaks. Seismic data collection lasted for exactly three weeks.

3.6.2 Layout of Profile Lines

The area covered was 31,200 m^2 (240 m x 130 m). Fourteen straight profile lines each of length 240 m running north to south were created with an inter-profile spacing of ten meters (figure 3.4). The end of the last four traverses were very close to the river creating shoting inconveniencies when carring out the seismic survey. Consequently, the last shotpoint of the last line was at 230 m instead of 240 m.

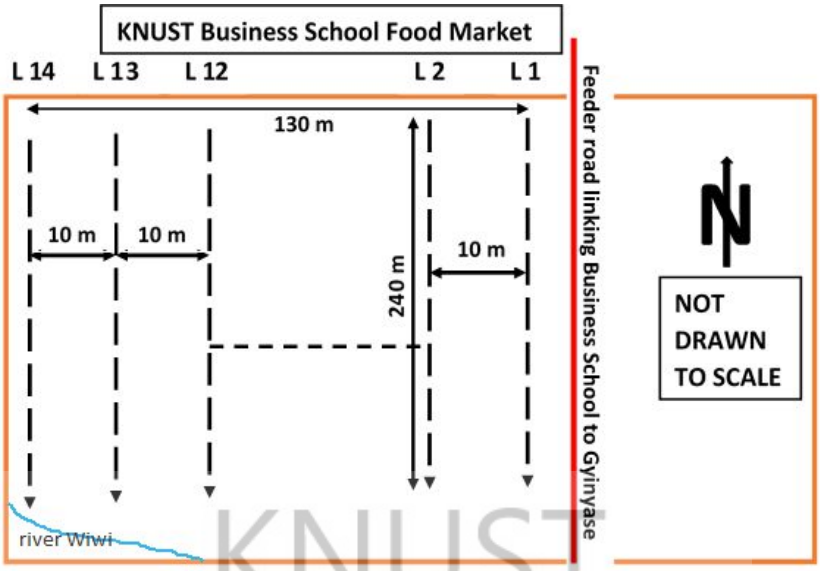

Figure 3.4: Layout of the profile lines at the site showing river Wiwi, Business School food market and the feeder road that links KNUST and Gyinyase.

3.6.3 Resistivity Data Acquisition

The ABEM SAS 4000 resistivity Lund imaging system was used in this work for resistivity data collection together with four multi-core cables (figure 3.5). Each of these cables is 40 m long has twenty-one take-outs with separations of 2 m. The ABEM SAS is used in carring out high resolution 2D electric imaging surveys using numerous electodes giving the operator the the chance in choosing protocols for a wide range of arrays like gradient, dipole-dipole, Schlumberger, Wenner, pole-dipole, square, pole-pole etc. It supports one- or four-channel operations. The device is powered with a 12 V car accumulator.

Forty-one steel electrodes were laid with separations of 4 m on a profile covering a length of 160 m. Take-outs on the cables were connected to the electrodes with the aid of jumpers. The multi-core cables 2 and 3 which are linked to 1 and 4 respectively were fixed on the electrode selector ES 10-64C connected to the resistivity device at the midpoint of the layout.

Figure 3.5: The ABEM Terrameter SAS 4000 device, electrode selector ES 10-64C and multi-core cables with their connectors.

To ensure continuity of the four cables, the last take-out of the previous cable and the first take-out of next cable were connected to the same electrode (take-out 21 and 1). This is a special characteristic of the ABEM lund imaging device used but not for other resistivity devices. Table 3.1 contains the neccessary acquisition parameters that were set for measurements.

Roll-along was employed to cover the 240 m profile length. This was achieved by disconnecting the first cable from the second after the first readings and connecting it to the fourth cable for the next readings. This covers a length of 200 m. The second cable was taken and connected to the last cable to make the 240 m length after the second data readings. In all cases the resistivity meter together with its sellector were moved to the centeral point of the four cables for measurement (figure 3.6).

Electrode coupling which is a usual problem in dc resistivity survey occuring in very loose or dry soils was experienced at most parts of the south-west. Poor coupling of electrodes is as a result of bad contact with the ground. This was taken care of by rehammering the failed electrodes to ensure better contact with the ground and adding water to enhance conductivity.

The ends of the profiles and cables were marked for proper location of electrodes as mislocation of electrodes can result in contamination adding misleading features to the inverted data (Oldenborger et al., 2005).

Figure 3.6: A setup of the ABEM Terrameter taking readings.

Table 3.1: Acquisition parameters used for apparent resistivity measurements.

Smallest electorde spacing	4 m
Power line frequency	50 Hz
Midpoint	40 (160 m)
Array type	Wenner Long
Output	200 mA
Acquisition delay	0.2 sec
Acquisition time	0.3 sec
Maxamum stack	4
Minimum stack	2
Error limit	1.0%
Data buffer size	20

3.6.4 Processing of Resistivity Data

The acquired data was processed using the Res2D INVERSION software. Measured apparent resistivity values are plotted in a psuedosection which take the form of a trapezium

showing the part of the subsurface covered. The data was edited taking off all bad data points before the inversion process. Bad data points include spiky and negative data which may have resulted from poor ground electrode contact, the presence of loose sandy soil or stony ground. The L_1 norm (robust inversion) which gives a more stable result (Dahlin and Zhou, 2004; Aning et al., 2013; Zhou and Dahlin, 2003) was employed using the Gauss-Newton method for the computation of the sensitivity matrix for all the iterations. The 2D data from the various lines were collated and inverted to generate a three dimenson model of the subsurface. The processing flow is shown in figure 3.7.

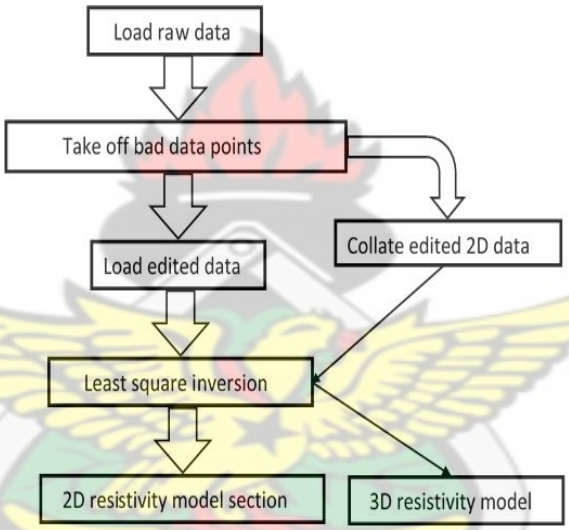

Figure 3.7: Flow chart of resistivity data processing.

3.6.5 Seismic Refraction Survey Design and Data Collection

The offset and other shots locations were carefully chosen considering the probing depth of this work. In seismic work, the depth of probe primary depends on energy of the source and length of the spread. Each profile line had two spreads (figure 3.8) to occupy the entire 240 m length. Five shot points were selected for each spread resulting in ten shot locations on a profile. The two offsets, the forward and reverse, were shot at 10 m before and after the first

and last geophones respectively. The inline shots were the central shot at the middle of the entire spread, the midpoint of the first twelve receivers and that of the last twelve receivers. The locations of the shots were 0 m, 37.5 m, 67.5 m, 97.5 m and 135 m on spread 1 and 105 m, 142.5 m, 172.5 m, 202.5 m and 240 m on spread 2.

For the sake of continuity, the two spreads were made to overlap thirty meters. This was done by leaving the last three geophones after shoting the first spread to serve as the first three receivers for the second spread.

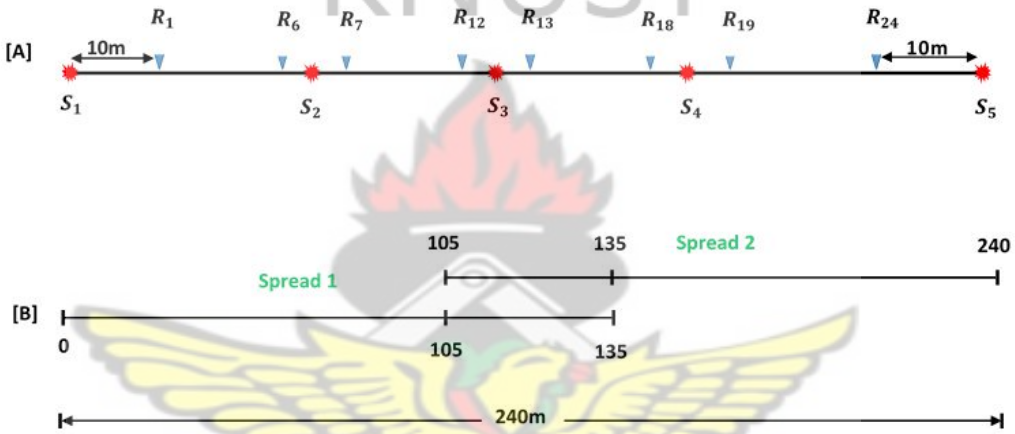

Figure 3.8: Design of the survey diagrams. [A] Shows the different shot locations S_1-S_5 and the some receiver positions, R_1-R_{24}. [B] Shows the two spreads on a profile line and the points of overlap.

Seismic data were collected with the ABEM Terraloc Mark 6 (figure 3.9). It is a twenty-four channel seismic recording system. The frequency of all the twenty-four geophones used as receivers is 10 Hz with a twenty pound sledge hammer as the source.

Figure 3.9: Pictures of the Terraloc Mark 6, refraction seismic cables and spiky 10 Hz geophone.

The receivers are electromagnetic geophones (figure 3.9). These are tranducers that convert the ground vibrations into electric signals which are recorded and saved by the seismograph as wiggles (figure 3.10). Electromagnetic geophone consist of a mass with wrapped strand wire placed in a magnetic field that is fixed to the Earth. Movement of the Earth causes the magnet to move up and down around the mass. The magnetic field of this moving magnet generates an electrical voltage in the wire which can be amplified and recorded by a simple voltmeter. The velocity of the ground movement can then be linked to the recorded voltage.

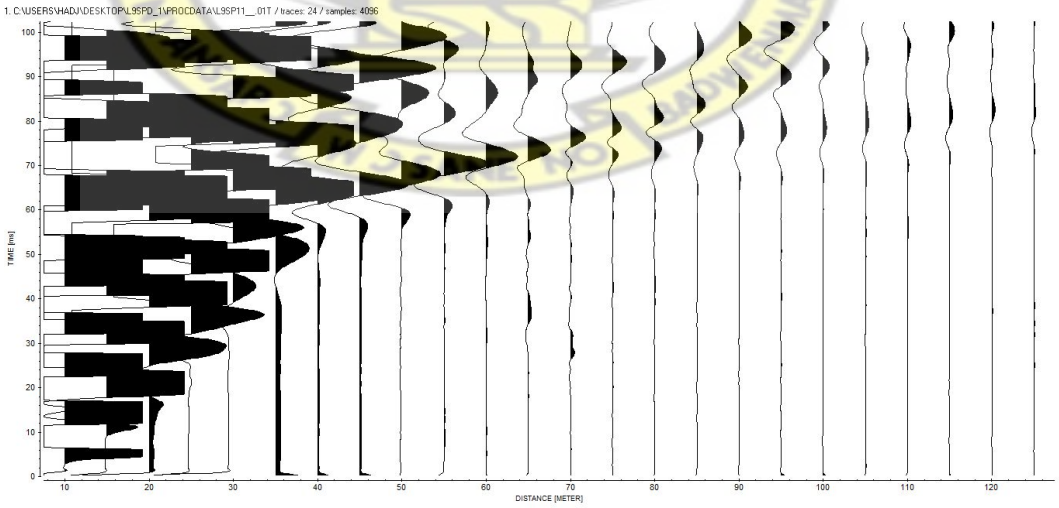

Figure 3.10: Forward shot unfiltered seismogram.

Twenty-four 10 Hz geophones with five meter separations were planted erect to the ground. The first was planted at the 10 m mark to give space for the ten meters forward offset shot with the last on the 125 m mark. The refraction cables connecting the receivers were connected to the terraloc placed at the middle of the spread. The position of the trigger geophone connecting to the recorder through the trigger cable was varied based on the shot location. The acquisition parameters in table 3.2 were used throughout the survey.

Table 3.2: Seismic acquisition parameters.

Sampling interval	25 μs
Number of samples	4096
Record length	102 ms
Number of stacks	3
Delay/Pre-trigger	10 ms
Stacking mode	Preview
Source type	Hammer
Receiver type	Vertical geophone
Cutoff frequency	48 Hz
Attenuation	12 dB
Measurement	standard

After all the required parameters were set, the trigger geophone was planted close to the metal plate at the shot point (figure 3.11) and connected to the trigger cable. The terraloc was armed and the receivers triggered after every shot.

Figure 3.11: Picture of a trigger geophone connecting the trigger cable beside a metal block at the shotpoint.

Three best seismic records of all the shots at a particular shot point previewed on the terraloc were selected for stacking and saved in SEG2 format. This was done for the other shot points.

All the geophones were taken off leaving the last three after the first spread. The geophones taken off were planted after the last three, now the first three, maintaining the same five meter separations to form the second spread. Figure 3.12 shows operators on the field with the ABEM Terraloc Mk.6 taking data.

Figure 3.12: Pictures of operator taking seismic measurement.

3.6.6 Seismic Data Processing

Seismic data was processed using ReflexW version 7 developed by Sandmeier (2008). This software employs the the intercept time analysis, tomography as well as raytracing for interpretation.

Processing refraction seismic data requires much care and experience as noise can be deceptive in picking first breaks. The main noise sources in the project environment were airplanes from the Kumasi airport and a water pumping machine used by the vegetable farmers for irrigation.

Using the 2D-data-analysis window of the ReflexW, a bandpass frequency of 15 Hz low cutoff and 300 Hz high cutoff were applied to take out the low and high frequency noise. These cuttoff frequencies were chosen considering the range of seismic frequencies (5 Hz-50 Hz) and observing the seismogram. In addition, a manual gain filter was also performed on the band filtered data. The gain function helped in revealing positions of the first arrivals much better (Sandmeier, 2008).

On a seismogram, the part of the wiggle where it deviates from being straight is the first break point (figure 3.13). As mentioned above, other amplitudes and breaks before the first break point may be deceptive and should be noted. First arrivals have very small amplitudes and are normally not sharp at the remote geophones. In a very noisy data, the first breaks occur just below the sharp waves with big amplitudes (shear waves).

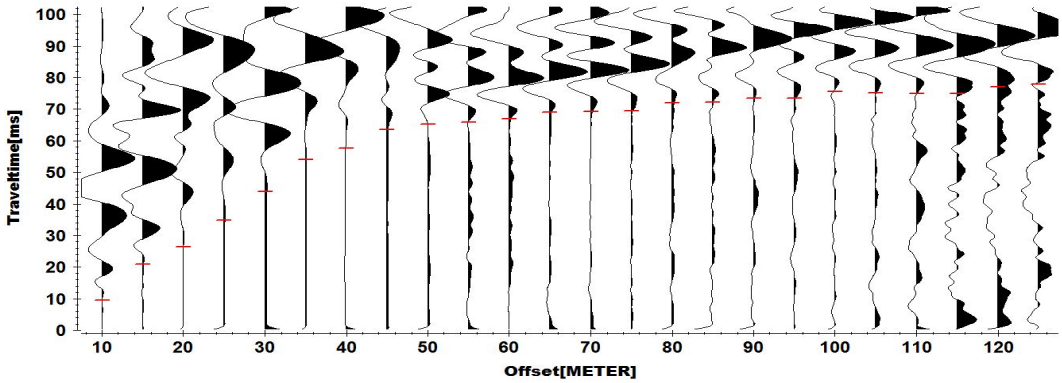

Figure 3.13: A seismogram with picked first breaks.

The first arrivals saved picks of the single shots on each traverse were combined in the traveltime-2D analysis window and assigned the various layer points. The part of a traveltime curve where any of the dotted-lines meet is the crossover point and indicate a change in velocity or density. Parallel to near parallel curves carry information from the same layer. The combined traveltimes curves were inverted directly using the wavefront inversion method into the underground model (Sandmeier, 2008). This model allows interactive back propagation of the wavefronts using finite differences approximation of the eikonal.

The eikonal equation is a non-linear partial differencial equation encountered in wave propagation problems, when the wave equation is approximated using the WKB theory (method for finding approximate solutions to linear partial differential equations with spatially varying coefficients). It can be derived from Maxwell's equations of electromagnetics, and gives a relationship between physical (wave) optics and geometric (ray) optics equation (Sethian and Vladimirsky, 2000; Gremaud and Kuster, 2006; www.wikipedia.org/wiki/Eikonal_equation, 2014).

$$|\nabla u(x)| = F(x), x \in \Omega \tag{3.1}$$

F(x) is a positive function, Ω is an open set and u(x) is the solution, thus the shortest time needed to travel from the boundary $\partial\Omega$ to x inside Ω, with F(x) being the time cost (not speed) at x.

The forward raytracing method used helped in validating the underground models derived from the wavefront inversion. Moreover, it gives correlation between the observed and calculated traveltimes hence improving the models. There is no need for approximations concerning the complexity of the models and makes this method very suitable for near surface investigations. Figure 3.14 describes the processing sequence of the refraction seismic data.

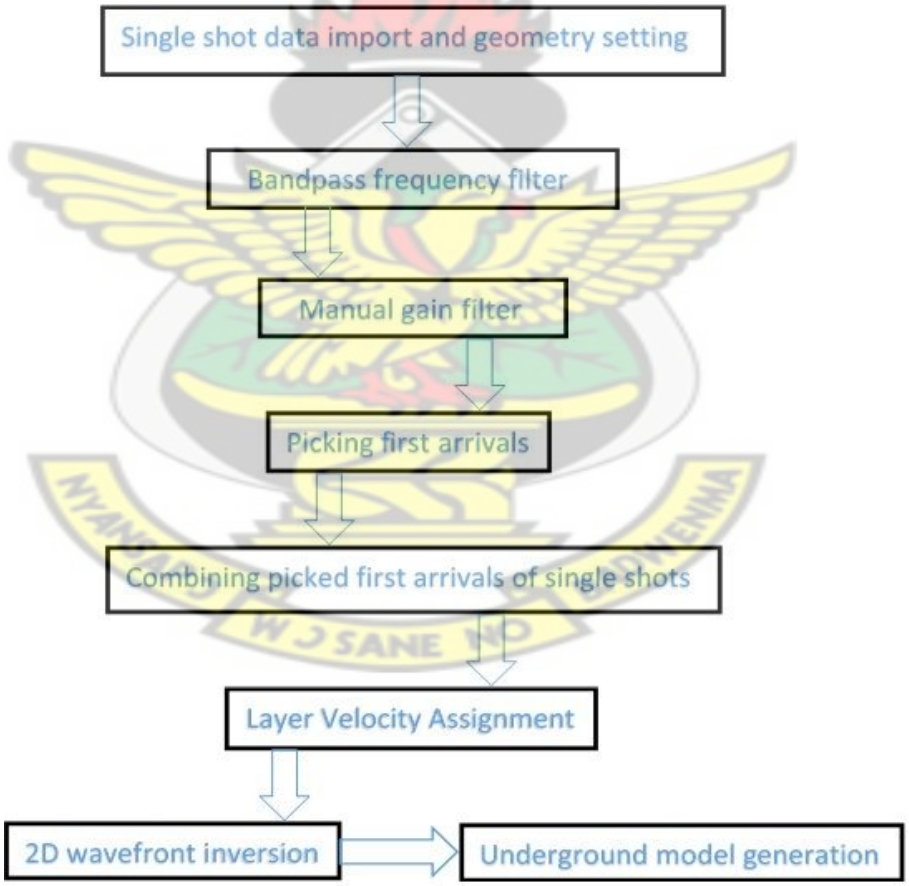

Figure 3.14: Flow chart of seismic data processing.

CHAPTER 4

RESULTS AND DISCUSSIONS

4.1 Introduction

In this chapter, the 2D apparent resistivity model sections obtained from each traverse are displayed showing the distribution of subsurface resistivity described in details. Each traverse 240 m long is oriented north-south with 10 m separations. A full version of the Res2DINV software was used to process all the resistivity field data. Depth of probe for the resistivity survey was approximately 27 m. The user defined contour option of the Res2DINV processing software was used to obtain same range of color shades for the 2D resistivity model sections for easy correlation. Also this chapter presents the geologic interpretation of the resistivity survey.

Presented in this chapter also is the qualitative and quantitative interpretations of the refraction seismic data. A fitted traveltime curve for the first single shot on profile one and all the velocity-depth models are displayed in this chapter.

For all the refraction seismic data obtained on the fourteen profiles, a full version 7 of the ReflexW 2D/3D interpretational software was used for processing. Depth to the bedrock and the bedrock's surface geometry was computed using the intercept time analysis.

4.2 Interpretation of Seismic Refraction

Relevant information required for the computation of thicknesses and the velocity of the near surface weathering layers which give indication of the geological structure on this basis are provided by refraction seismic surveys. Typically in long offset seismic reflection surveys, refractions are used to obtain the velocity structure of the subsurface (Cox et al., 1999; Ahmad et al., 2009). According to Cox et al. (1999), the velocity and weathered layer thickness derived from seismic refraction are essential for static correction.

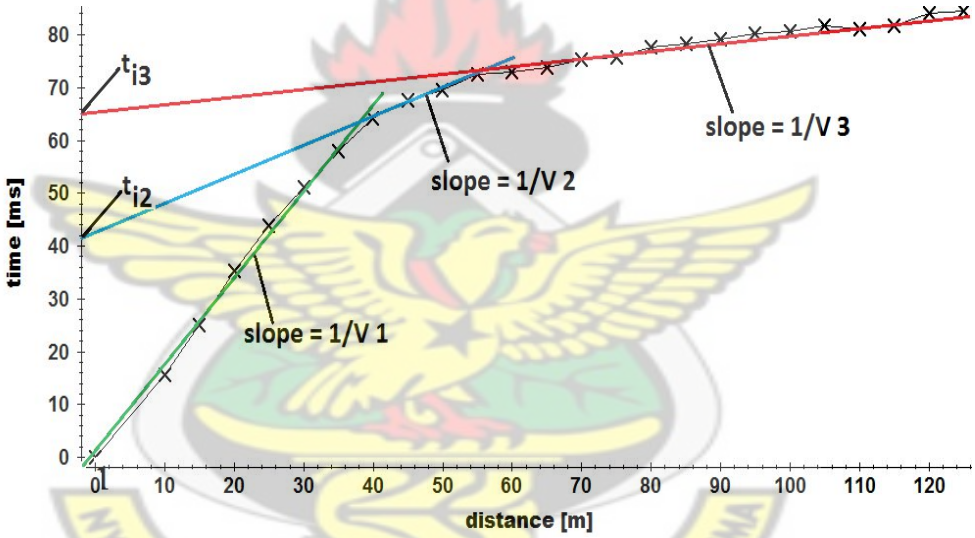

Figure 4.1: Traveltime curve for forward shot of profile 1 spread 1 showing direct waves in green and refracted waves in blue and red.

Seismic refraction make use of the traveltime of the waves arriving first at the geophones from the source. Data interpretational method may be chosen depending on the complexity of the geologic setting. The intercept-time analysis, plus-minus method by Hagedoorn or the tomography technique (good for soils with high lateral velocity variation) can be used for seismic refraction interpretation. Here, a reverse profile was carried out employing the intercept-time method of interpretation.

Traveltime curves of the forward and reverse profiles are the same for horizontal interfaces but differ for undulating/dipping refractors. The traveltime of the first arrivals at the receivers were plotted against their corresponding distance from the source (figure 4.1). Parts of the traveltime plot where there is a bend represent crossover points and indicate change in acoustic impedance. Plane refractor interfaces produce a straight or nearly straight refraction curves. If the refractor is undulating, the refraction curve is linked by scattered velocity points. Traveltime curves derived from properly picked first breaks on a seismogram show an offset in the refracted arrivals for an environment with faulting in the subsurface. The extent of the offset in the refracted line can give a fair idea of how much the two halves of the faulted formation are displaced.

In the intercept-time interpretational method, a simple geology and a horizontal refractor is assumed. One major shotcoming of this interpretational method is its inability to efficiently account for lateral velocity variation. Both the direct and refracted curves were fitted and their slopes and intercept time computed using linear regression (equation 4.1 and 4.2). The velocity of the layers delineated are the reciprocal of the slope of their curves given by equations 2.7 and 2.8.

All the velocity-depth models showing the levels of weathering at the site were generated with the inversion of the combined traveltime curves of all the shotpoints of the two spreads on a given profile assigning it the right layer velocity. Differences between the forward and reverse shots of the combined and assigned traveltime curves for all the spreads were less than 3.0 (figure 4.2). This shows a good layer assignment in generating stratigraphic models of the underground. Computation of the true layer velocities taking into account the geometry of the refracting interfaces follow equations 2.7, 2.8, 2.17, 4.1 and 4.2. Where x = offset, y = arrival time, n = number of data points to be fitted and m = gradient of the line of

best fit.

$$slope(m) = \frac{n\Sigma(xy) - \Sigma(x)\Sigma(y)}{n\Sigma(x^2) - (\Sigma(x))^2} \tag{4.1}$$

$$intercept(c) = \frac{\Sigma(y) - m\Sigma(x)}{n} \tag{4.2}$$

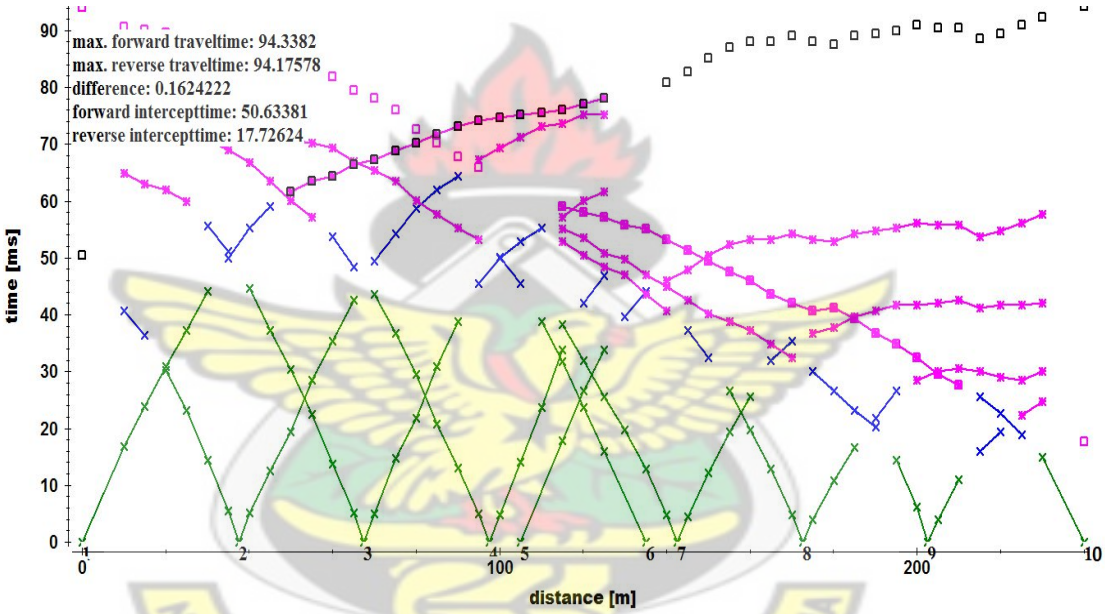

Figure 4.2: Combined traveltime curves of profile 6 showing an error margin of 0.1624222 for underground model generation. Green lines for layer one, blue lines for layer two and pink lines for layer three assignment.

The refraction seismic survey revealed three acoustic layers showing the stratigraphy of the study area (figure 4.3).

Dry rocks have their pore spaces filled with air and have low elastic velocity. Also, poorly consolidated rocks and disseminated soils may have strong absorbtion of shear waves if they do not respond elastically (Milsom, 2007). For very dry unconsolidated overburdens, p-wave

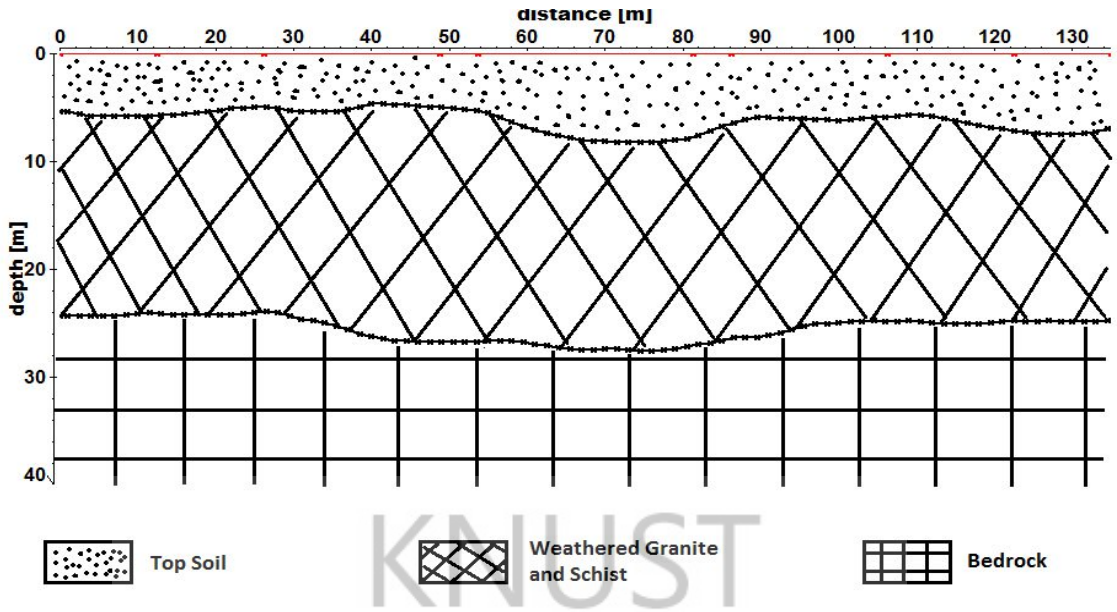

Figure 4.3: Stratigraphic diagram of the study area.

velocity can be as low as speed of sound in air (330 m/s) or even less. Poorly consolidated soils hosting high amount of water have velocity slightly greater that of speed of sound in water (Milsom, 2007). Hence the influence of fluid being water, air or oil on the seismic velocity of materials cannot be understimated. Furthermore, weathering also has a marginal reduction in the velocity of rocks by increasing its pore content. This condition reduces the rippability of rocks and is a major concern to the geotechnical engineer especially on mountaineous areas.

At deeper depths, layers with low velocity will not give rise to critically refracted head waves. Also in seismic refraction surveys, high-velocity thin layers cannot be detected. Refracted waves within such geologic feature rapidly lose energy with increasing distance from the shotpoint and makes it blind. Direct measurement of vertical velocity may reveal such zones.

Generally, most pristine bedrocks have p-wave velocity greater than 2500 m/s (Milsom, 2007). In this work, a weathered zone which has velocity range between 1189-1450 m/s overlays the bedrock which has velocities > 3700 m/s.

4.3 Interpretation of Resistivity Results

Basically the electrical properties of soil and rocks that form the Earth's crust are determined by factors such as porosity, permeability, tempareture, clay and water contents (Loke, 2001). High weathering in rocks increases the porosity as well as permeability. These two factors give more room for water to find its way into soils and rocks aided by gravity. Water conducts electrolyticaly and therefore causes reduction in the resistivity of rocks. In water-bearing rocks, the presence of clay minerals boost conductivity as a result of the ion-exchange process in clay. Sometimes, particles of clay coating on the surfaces of rocks may affect the rock's bulk resistivity (Ward, 1990; Andrews et al., 2013; Revil and Glover, 1997). Increase in tempareture causes ions to move faster thereby enhancing the subsurface conductivity (Keller and Frischknecht, 1966). This effect is very minute and negligible in most environments as tempareture variation in the subsurface is small but cannot be ruled out in permafrost regions (Aizebeokhai, 2010). According to Campbell et al. (1948), conductivity increases by 2.02 % per ^{O}C between 15 and 30 ^{O}C.

Geologic inference drawn from resistivity surveys must be done with a lot of considerations such as geologic information of the area under study (Kesse, 1985), external features at the site and reviewing similar work by other authors as there is no fixed resistivity for soils and rocks of the Earth crust. In this work, geologic implications of the range of resistivity values obtained from the 2D apparent resistivity model sections have been presented in summary on table 4.1 and also further discussed below.

Table 4.1: Geologic interpretation of resistivity values obtained for this work.

Resistivity (Ω.m)	Description
50-200	Clay or saturated zone
200-600	Sandy-clay formation or lateritic soil
600-1600	Hard zone and fairly weathered bedrock
> 1600	Loose sand at surface, very hard zone or rock at deeper depths. Possibly an air-filled void if confined.

Clay/Saturated Zones

Clay conducts and sometimes may creat an impression of groundwater on resistivity model sections if it is moist. Very low resistivity values in the range of 50 to 200 Ω.m found on the 2D apparent resistivity model sections about 4 m below the surface and also at deeper depths could be clay or water saturated zones. This sort of resistivity at the begining of the profile lines is mainly due to clay. These resistivity values occuring close to the end of the 2D resistivity model sections are probably as a result of clay at the surface to depths of about 4 m and saturated clay at depths > 4 m.

Sandy-clay/Laterite Soil

Portions of the 2D apparent resistivity model sections with low resistivity between 200 and 600 Ω.m probably represents sandy-clay formation or laterite soil. This range of resistivity occurs at both shallow and deeper depths in the subsurface on all the 2D apparent resistivity model sections. At shallower depths (< 5 m) beneath the surface, these resistivity values may be as a result of lateritic soils but represent highly weathered besides weak zone at deeper depths.

Hard Zones

On the 2D apparent resistivity model sections, moderately high to high resistivity, 600 to 1500 Ω.m, suggest resistive hard and more compact zones. In addition, it also suggest minor

weathered part of the bedrock if it occurs just on top of it. This parts of the subsoil are competent and have high capacity to hold the weight of giant structures.

Loose sand/Very hard zones/Rock

Parts of the 2D apparent resistivity model sections display very high resistivity ranging between 1600 and 3000 Ω.m. These resistivity values occuring on the surface to depths < 2 m probably may be dry and highly desseminated mixture of sand and alluvium deposits with pore spaces filled with air. Air have infinite resistivity and its presence in a porous medium may cause increase in apparent resistivity. Also at deeper depths, these resistivity values suggest a very hard zone which represents the bedrock with a fairly weathered top.

Possible Void

On an apparent resistivity model section, a faulted zone appears as a continuous formation with a sharp slip up or down. It can also be identified as a very high or very low resistive thin zone depending on the infill within a formation (Aning et al., 2013). This also applies to voids. According to Sheets (2002), very high localized resistivities on a 2D resistivity model section deviates from normal geologic materials. The 2D apparent resistivity model sections obtained for this work show portions with confined high resistivity greater than 1500 Ω.m. These confined regions with very high resistivity could possibly be voids filled with very loose sediments and air.

4.4 Results of Resistivity and Seismic Refraction Surveys

4.4.1 Profile One

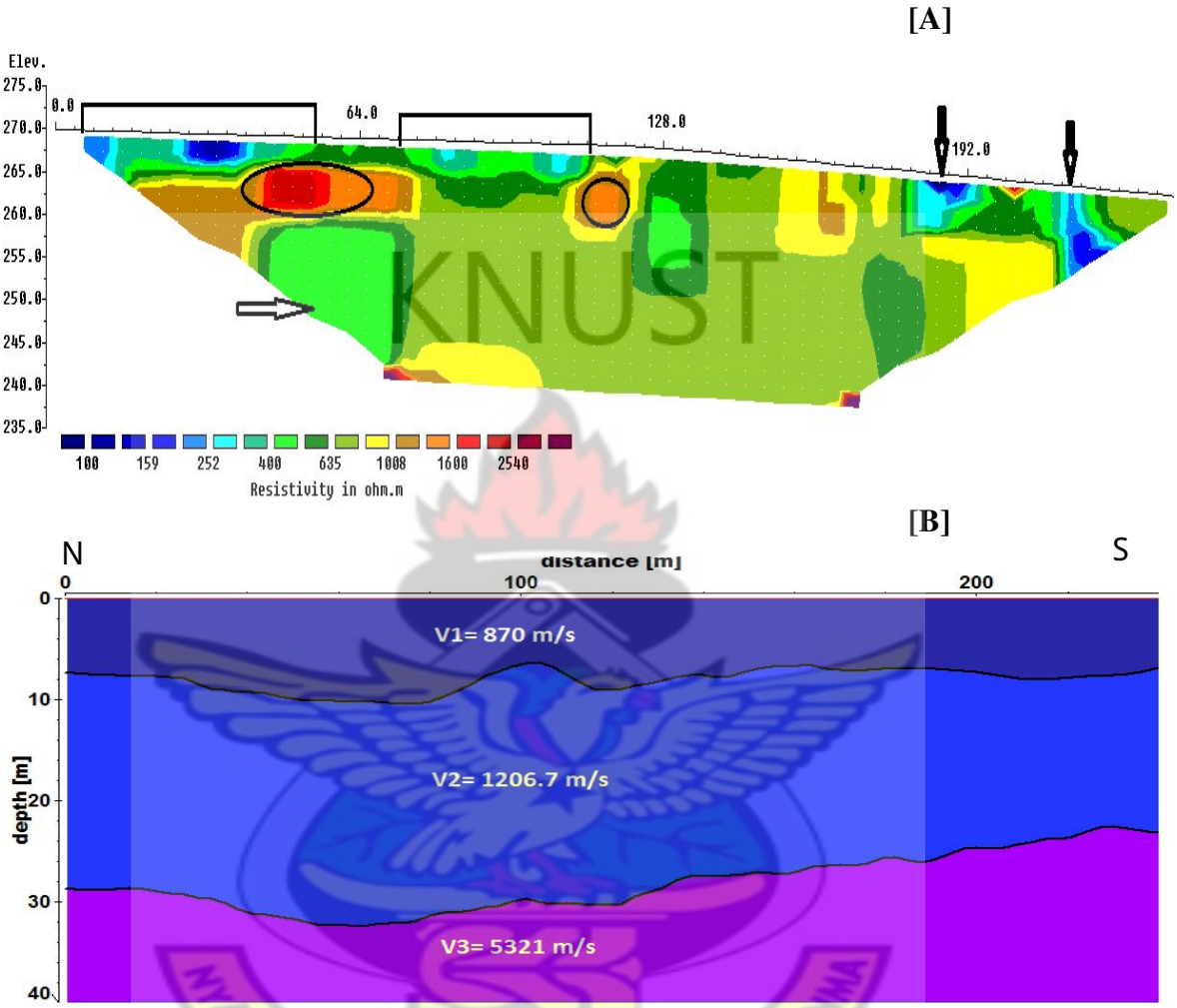

Figure 4.4: 2D apparent resistivity model section and velocity-depth model of profile 1.

Low resistivity regions (< 600 Ω.m) on the apparent resistivity model section of profile 1 (figure 4.4 [A]) can be found from the begining of the profile to 56 meters, 72-112 meters, 180-196 meters and 204-220 meters. These low resistive regions extend to depths of about 5-7 m with later trending deep into the subsurface. Another low resistive region occurs at a depth of about 10-26 m from 44-72 meters. Most of the central portions show dominant moderately high resistivity. Confined resistivity > 1500 Ω.m can be found about 5 m below

48 and 118 meter.

The velocity-depth model of profile one (figure 4.4 [B]) shows quite uniform velocity with an average of 870 m/s and thickness of about 8 m for the first layer. The second layer recorded an average elastic wave velocity of 1206.7 m/s in a depth range of 8-28.6 m. Velocity of 5321 m/s, a signature of the hard underlying bedrock on this profile was found at depth greater than 28.6 meters for layer 3.

4.4.2 Profile Two

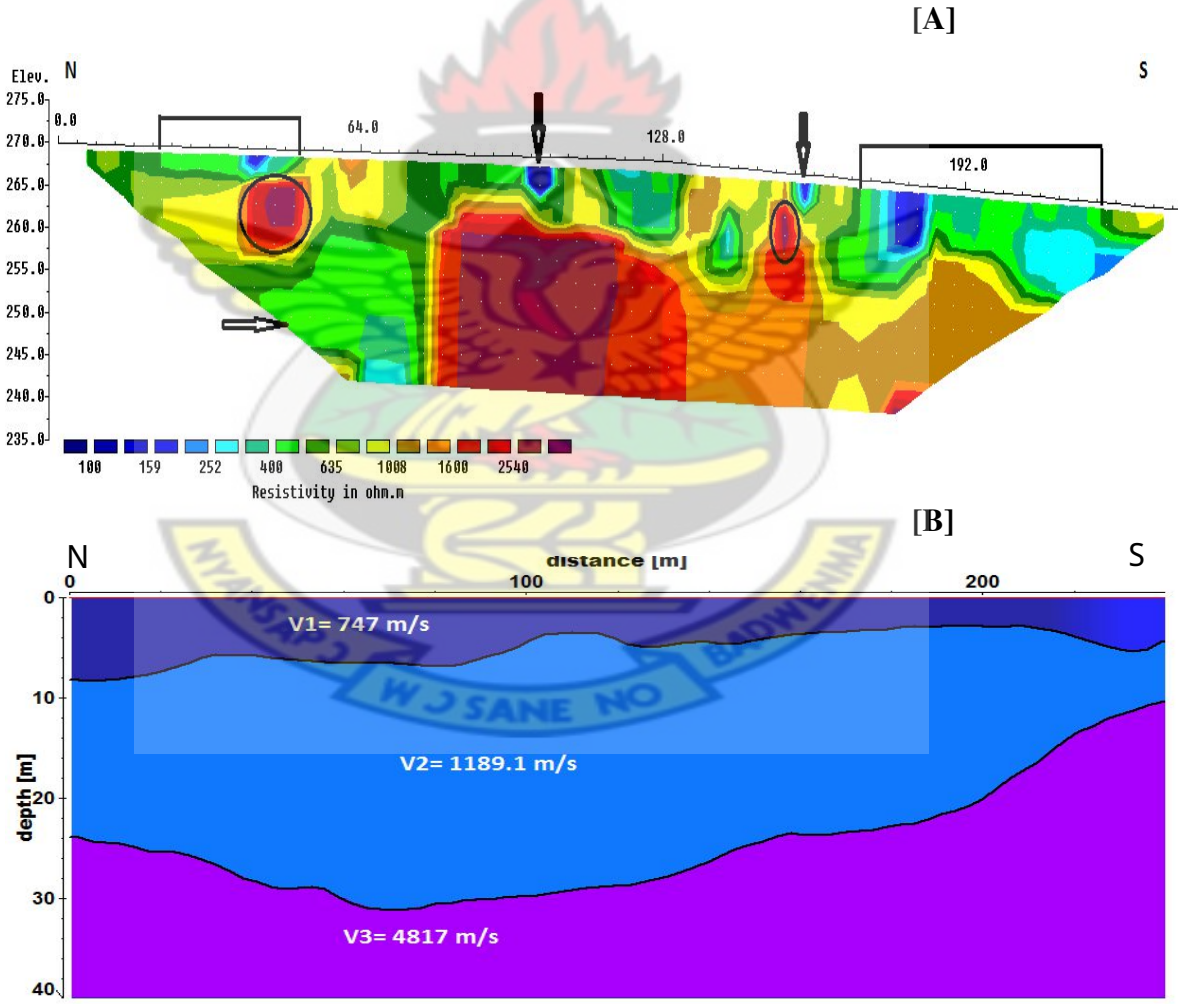

Figure 4.5: 2D apparent resistivity model section and velocity-depth model of profile 2.

The apparent resistivity model section of line 2 (figure 4.5 [A]) displays low resistivity

portions (< 600 Ω.m) from 20-56 meters, 80-100 meters, 116-132 meters and 170 meters in the subsurface to depths of 4-7 m. The latter is about 15 m deep in the subsurface. Portions of localized high resistivity (> 1500 Ω.m) are located at 5 m beneath 44 and 152 meter. The centeral parts of this resistivity model section exhibit very high resistivity > 1500 Ω.m from depths of about 7 m to 26 m.

Layer 1 of the velocity-depth model of line 2 (figure 4.5 [B]) has an average velocity of 747 m/s and thickness of about 7 m. Layer 2 has average velocity of 1189.1 m/s. The third layer recorded an average velocity of 4817 m/s and delineated > 26 m at begining of the line and 15 m at the profile end.

4.4.3 Profile Three

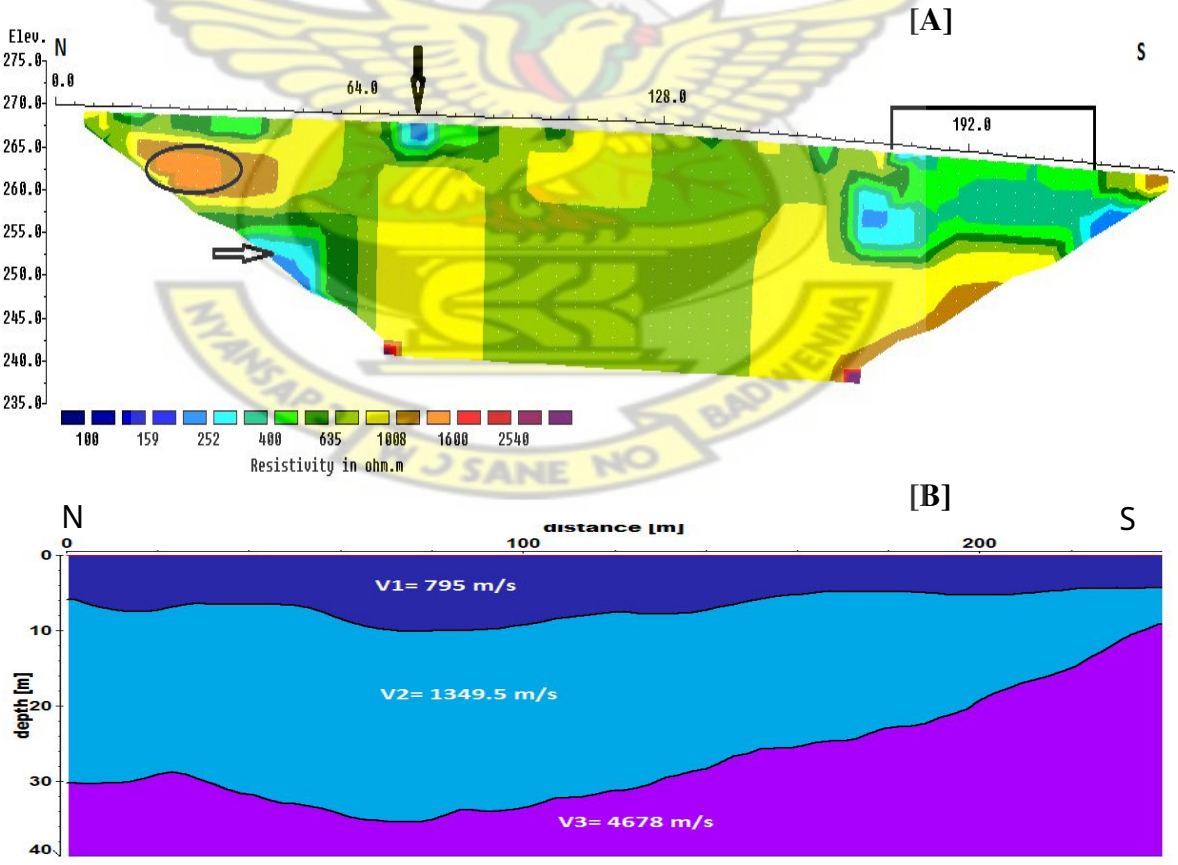

Figure 4.6: 2D apparent resistivity model section and velocity-depth model of profile 3.

Profile 3 displays moderately high resistivity in the central parts on the resistivity model section (figure 4.6 [A]). Patches of low resistivity occur at 16 meters, 32 to 44 meters and 160 meters in the subsurface to depths of 3-5 m. There is also a low resistive region that extends about 15 m deep into the subsurface from 168 to 220 meters. A confined high resistivity (1700 Ω.m) is located 5 m below the 28 meter.

The first layer of the velocity-depth model of profile 3 (figure 4.6 [B]) recorded an average velocity of 795 m/s with an average thickness of 6 m. Layers 2 and 3 have velocities of 1349.5 m/s and 4678 m/s respectively. Layer 3 occurs at depths > 30 m at the begining of the profile and > 12 m at the end of the profile.

4.4.4 Profile Four

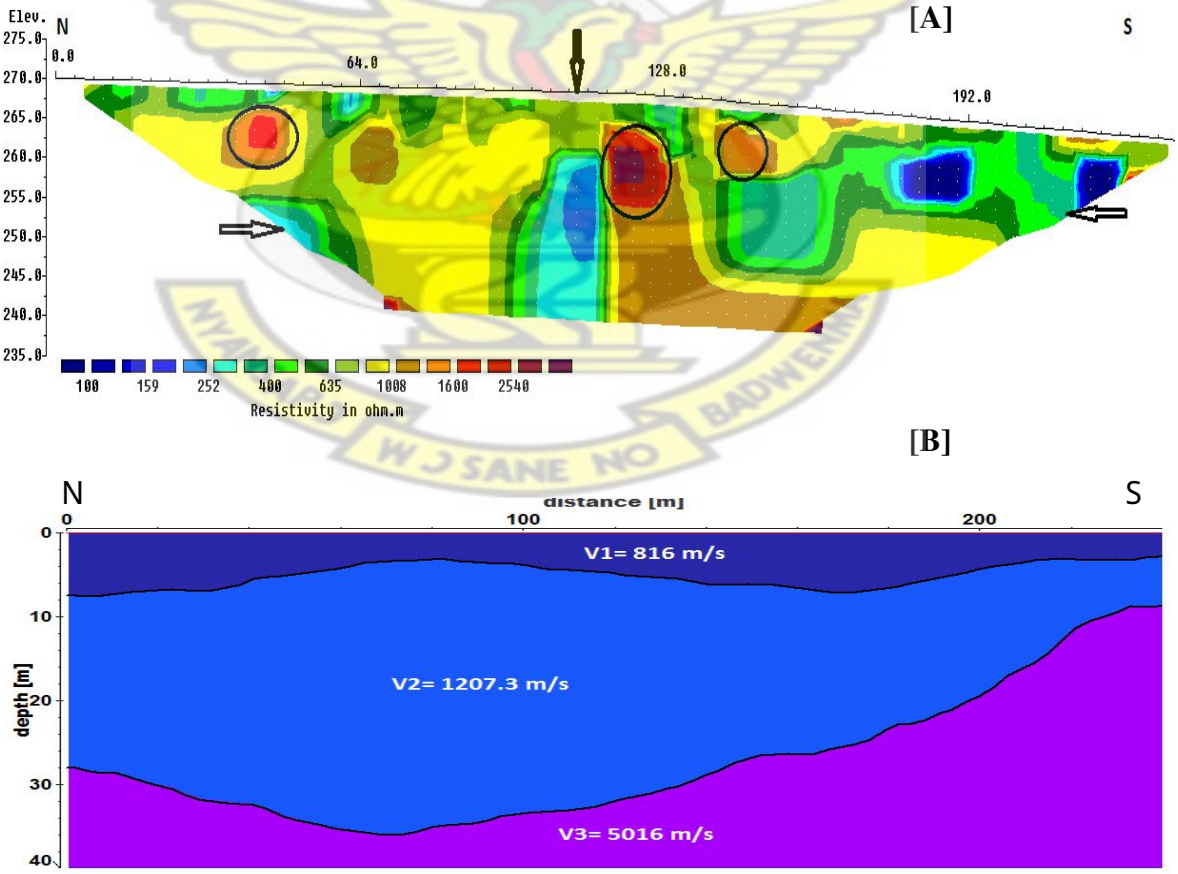

Figure 4.7: 2D apparent resistivity model section and velocity-depth model of profile 4.

On the apparent resistivity model section for line 4 (figure 4.7 [A]), low resistivities (< 600 Ω.m) are found at 14 meters, 24 to 48 meters, 56 to 68 meters, 96 meters, 124 to 132 meters and 144 meters. Other low resistive regions are located at 94-106 meters from about 7 m to 26 m depth and also from 140 meters to the profile end 10 m in the subsurface. Confined high resistivity regions (> 1500 Ω.m) 4 m deep in the subsurface are encountered at 44, 120 and 144 meters.

The velocity-depth model of line 4 (figure 4.7 [B]) has average velocities of 816 m/s, 1207.3 m/s and 5016 m/s for layers 1, 2 and 3 respectively. Averagely, layer 1 is 6 m thick. Layer 3 is buried at depths > 30 m at the begining of the line and > 15 m at the end of the profile.

4.4.5 Profile Five

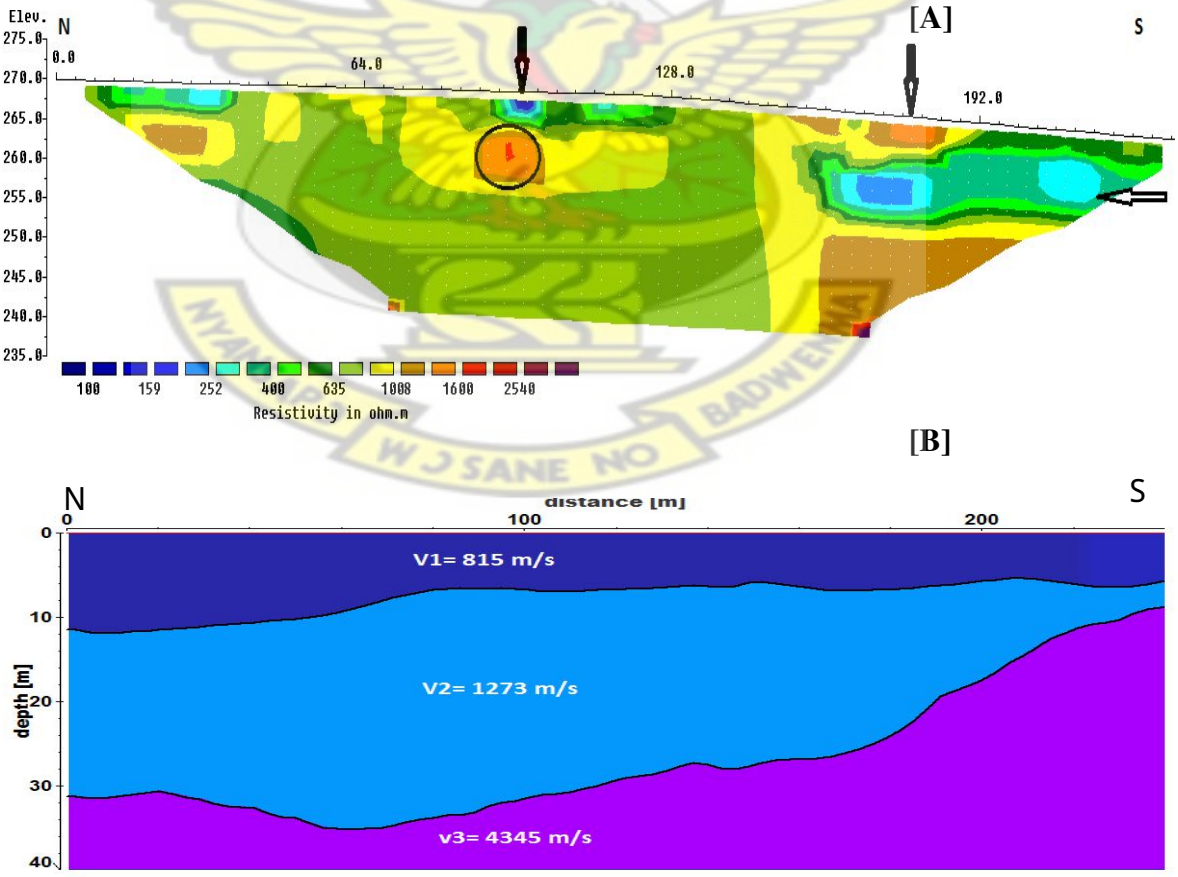

Figure 4.8: 2D apparent resistivity model section and velocity-depth model of profile 5.

Low resistivity (< 600 Ω.m) can be found at 12 to 36 meters and 86 to 124 meters on the apparent resistivity model section (figure 4.8 [A]). The central portions are dominated by moderately high resistivity > 600 Ω.m.

On the velocity-depth model for line 5 (figure 4.8 [B]), average velocities of 815 m/s, 1273 m/s and 4345 m/s were recorded for layers 1, 2 and 3 respectively. The third layer is buried 32 m deep in the subsurface at begining of the line and about 12 m at the profile end.

4.4.6 Profile Six

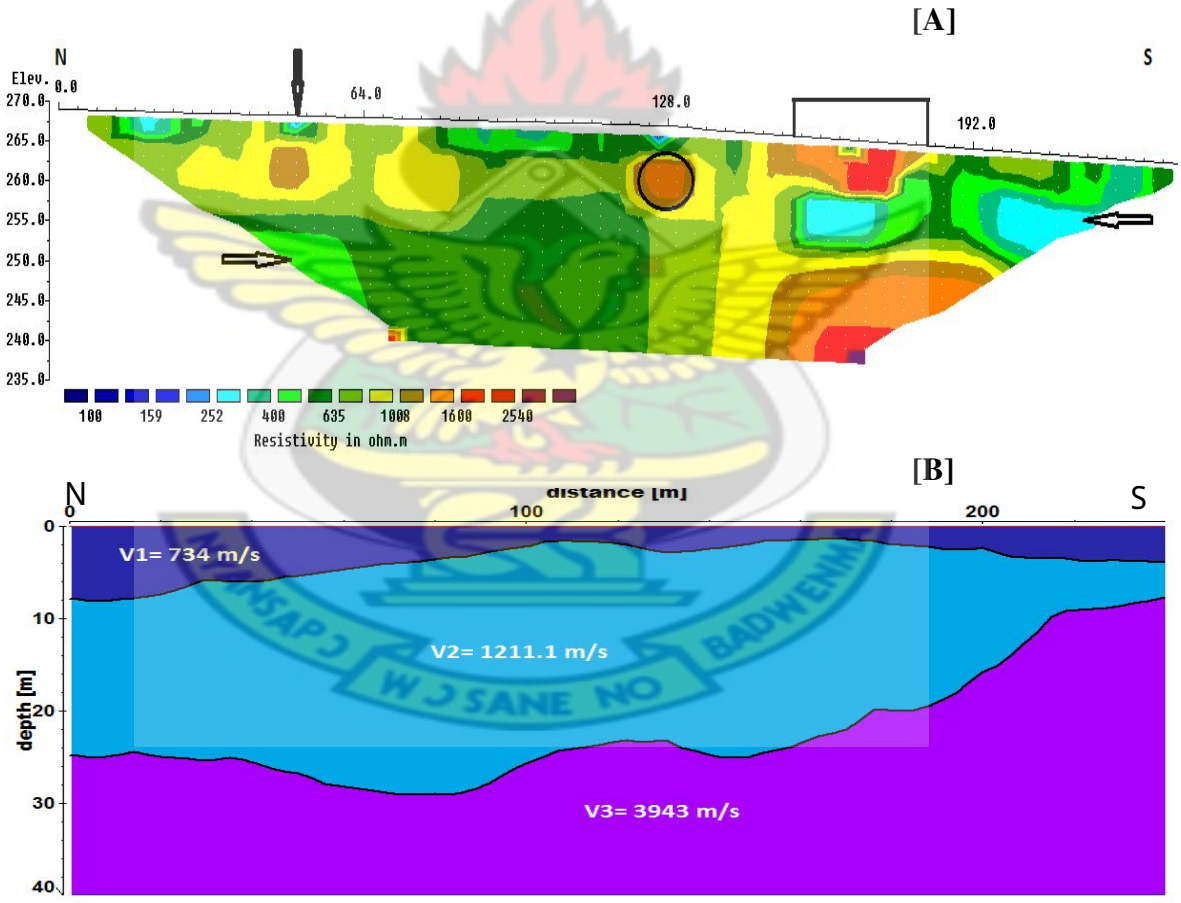

Figure 4.9: 2D apparent resistivity model section and velocity-depth model of profile 6.

The apparent resistivity model section of line 6 (figure 4.9 [A]) has a low resistive region below a very high resistive subsurface 7 m thick from 152 meters to the end of the profile.

These low resistivities (< 600 Ω.m) also occur as patches at 12 to 26 meters, 50 meters, 80 to 108 meters and 126 meters to depths of 4 m in the subsurface. A confined high resistivity (1600 Ω.m) is found about 5 m below 126 meters.

The average velocities on the velocity-depth model of line 6 (figure 4.9 [B]) for the first, second and third layers respectively are 734 m/s, 1211.1 m/s and 3943 m/s. Layer 1 is very thin about 1.5 m from 100 to 200 meters and increases in thickness from 100 meters to the begining of the line. Layer 3 was delineated at depths > 25 m at the begining of the line and > 12 m at the end of the profile.

4.4.7 Profile Seven

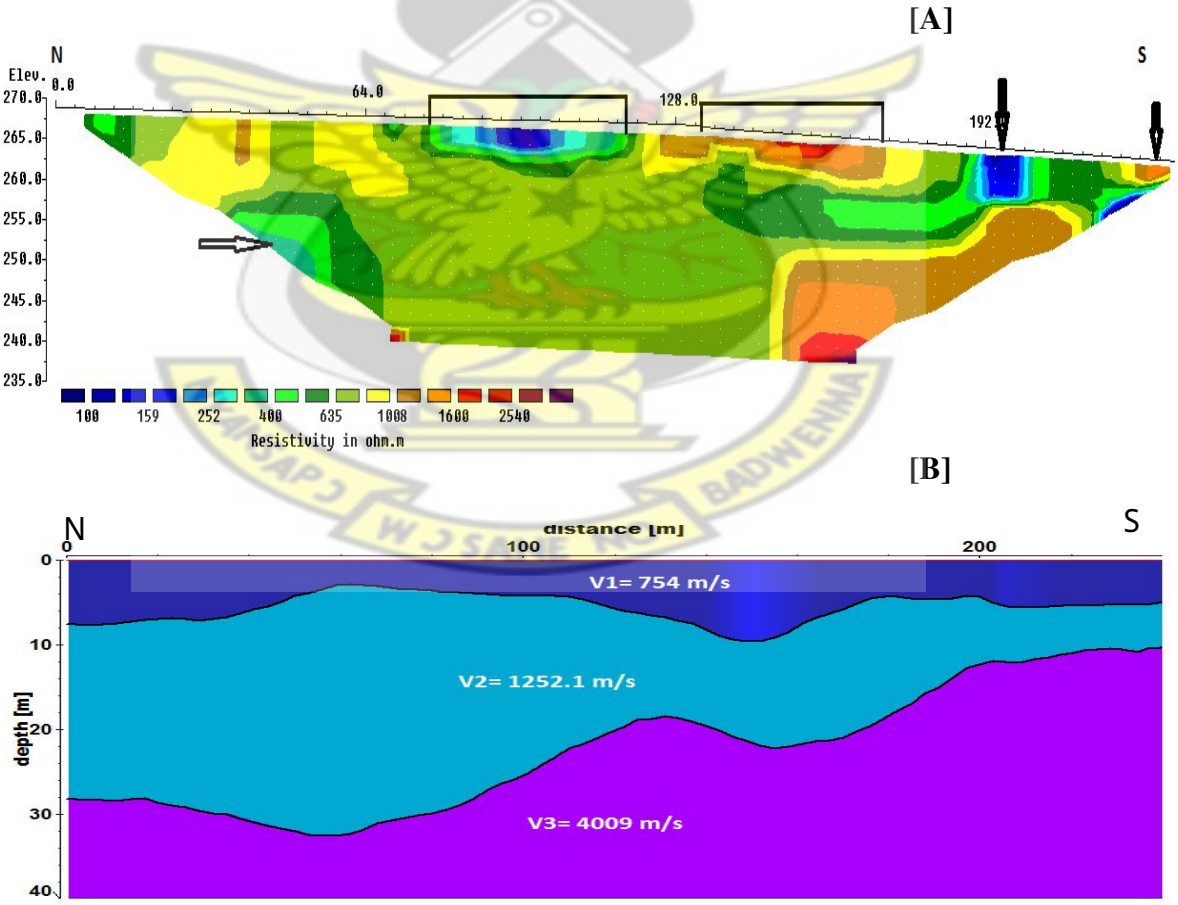

Figure 4.10: 2D apparent resistivity model section and velocity-depth model of profile 7.

Profile seven displays uniform distribution of moderately high resistivity in the central portions on the resistivity model section (figure 4.10 [A]). The subsurface exhibit high resistivity from 136 to 168 meters to depth of 5 m. Low resistive region between 188 and 204 meters trends 15 m deep into the subsurface. Others low resistive zones occur at the begining of the profile and also at 76-120 meters to depths of about 5 m.

The velocity-depth model of line 7 (figure 4.10 [B]) has an average layer 1 velocity of 754 m/s. Layer 2 and 3 have velocities of 1252.1 m/s and 4009 m/s respectively. Layer 3 was mapped at depths > 15 m deep at the profile end and dips downwards to 30 m at the begining of the line.

4.4.8 Profile Eight

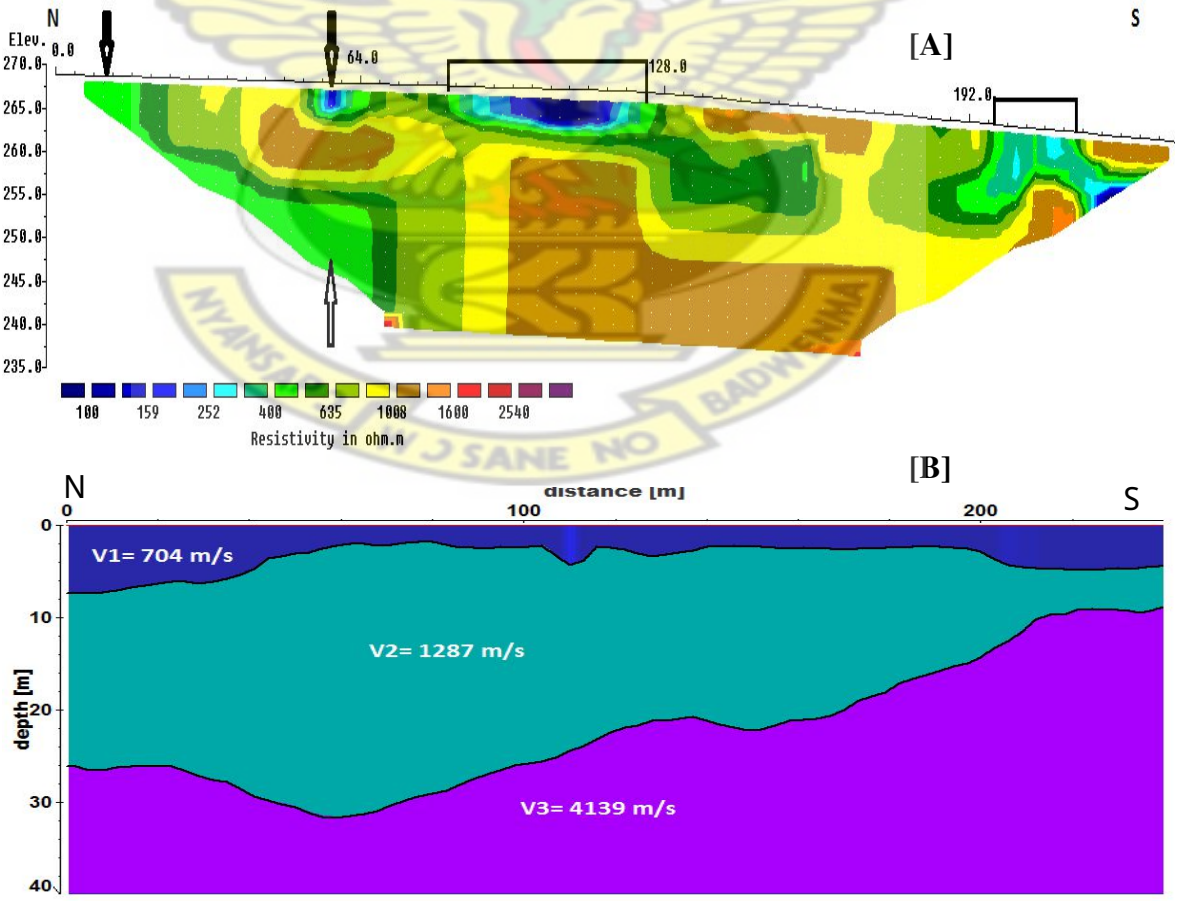

Figure 4.11: 2D apparent resistivity model section and velocity-depth model of profile 8.

The apparent resistivity model section for profile 8 (figure 4.11 [A]) has low resistive zones (< 600 Ω.m) located at the begining of the line to 22 meters and 196-204 meters extending to depths of 25 and 15 m respectively. Other low resistive zones in the subsurface are found at 52 to 66 meters and 76 to 128 meters about 7 m deep. The central parts exhibits moderately high resistivity > 600 Ω.m.

Layer 1 of the velocity-depth model for line 8 (figure 4.11 [B]) is about 4 m thick with average velocity of 704 m/s. Layer 2 and 3 have average velocities of 1287 m/s and 4139 m/s respectively. Layer 3 is buried > 29 m deep at the begining of the profile and also > 12 m deep at the end of the line.

4.4.9 Profile Nine

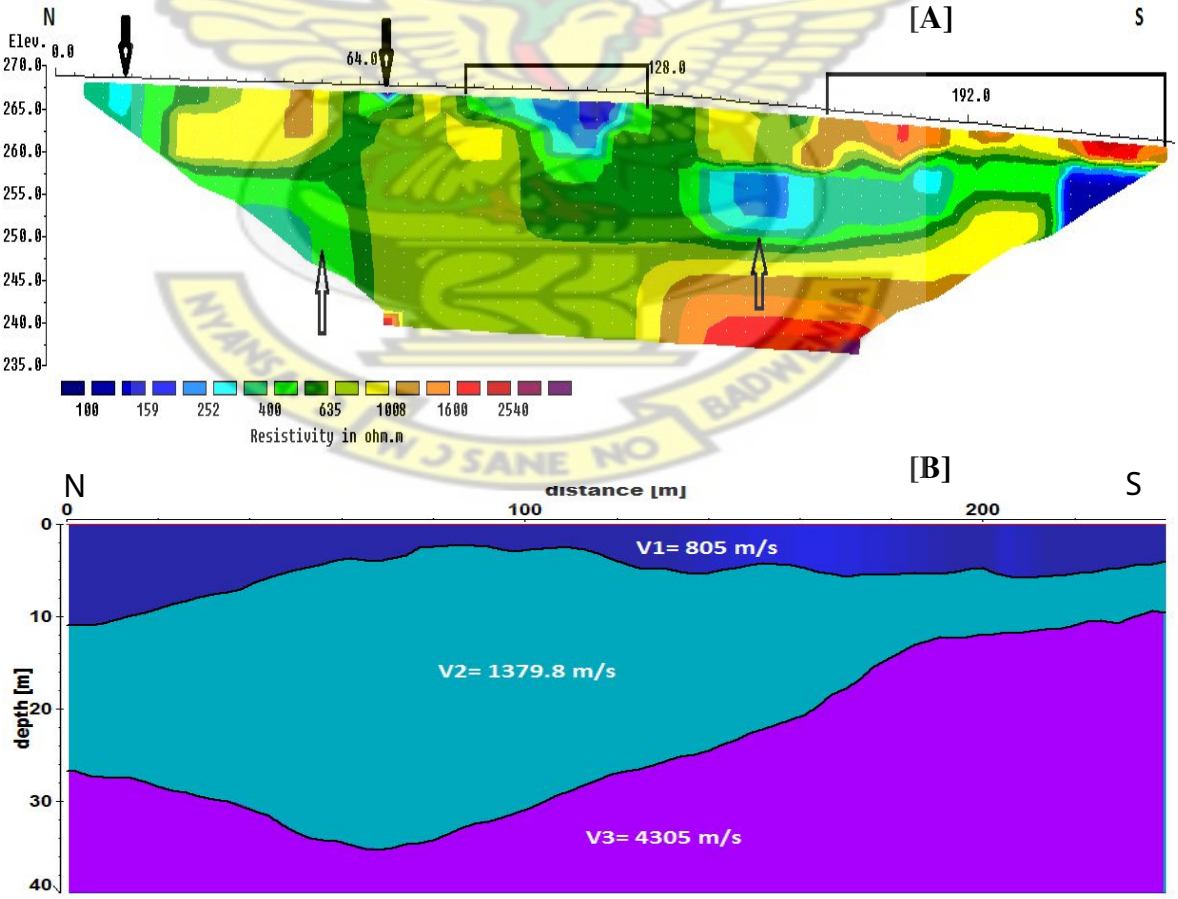

Figure 4.12: 2D apparent resistivity model section and velocity-depth model of profile 9.

The apparent resistivity model section of profile 9 (figure 4.12 [A]) shows low resistive zone from the begining of the line to 22 meters that extends to 25 m depth. Low resistive zone can also be found at 84 to 126 meters in the subsurface to 15 m depth. The subsurface from 136 meters to end of the line displays high resistivity to depth of about 6 m. Below this zone is a low resistivity zone that becomes more resistive beyond 20 m.

Figure 4.12 [A] is the velocity-depth model of line 9 and has an average velocity of 805 m/s, 1379.8 m/s and 4305 m/s for layers 1, 2 and 3 respectively. Layer 1 is about 6 m thick. Layer 3 is about 14 m deep at the end of the line but was delineated at depths > 30 m at the begining of the profile.

4.4.10 Profile Ten

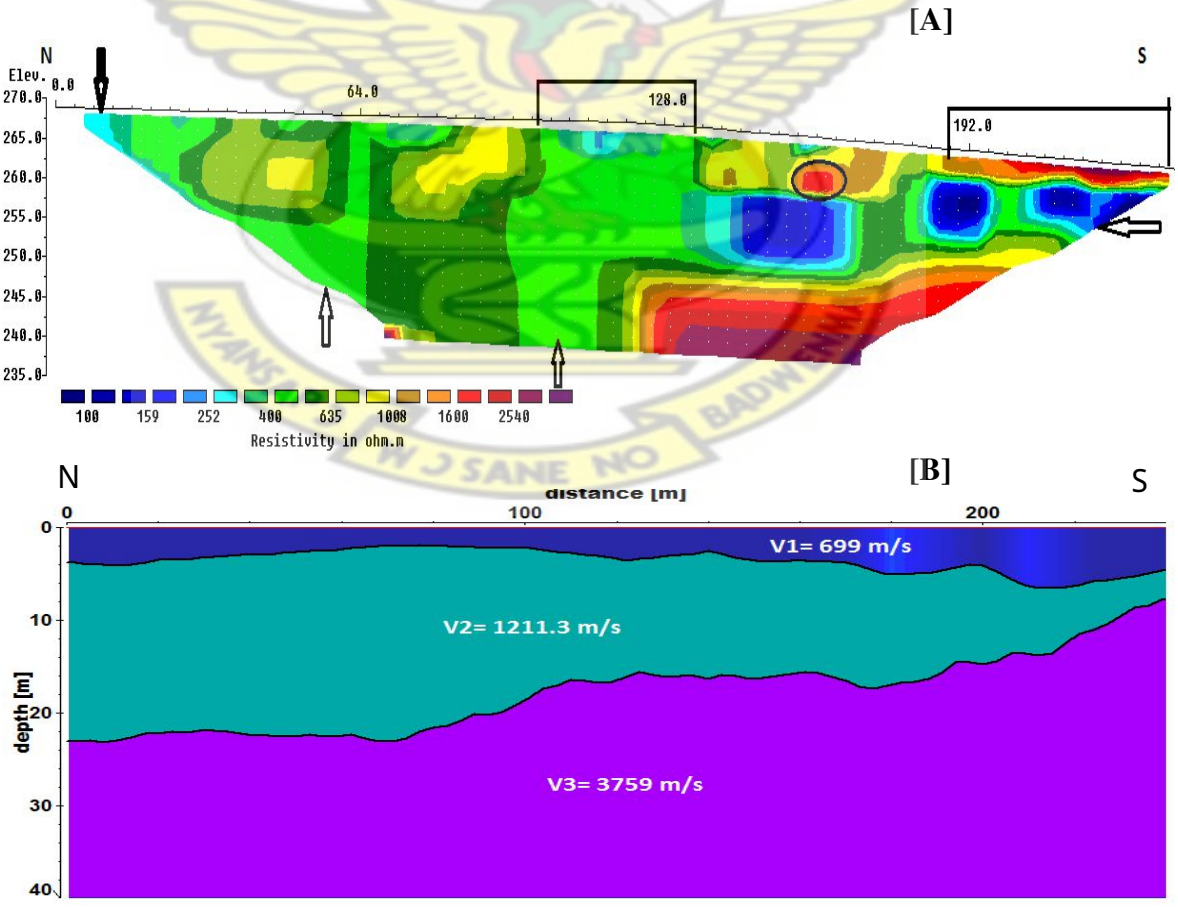

Figure 4.13: 2D apparent resistivity model section and velocity-depth model of profile 10.

The apparent resistivity model section of profile 10 (figure 4.13 [A]) has low resistivity (< 600 Ω.m) from the begining of the line to 132 meters that extends to depths of about 27 m in the subsurface. The subsurface from 140 to 190 meters to depth of 6 m shows moderately high resistivity and becomes highly resistive from 190 meters to the end of the line. Below this high resistive zone is a 10 m thick low resistive zone seated on a region with very high resistivity (> 1500 Ω.m).

Layers 1, 2 and 3 of the velocity-depth model of line 10 (figure 4.13 [B]) have average velocities of 699 m/s, 1211.3 m/s amd 3759 m/s. Layer 1 is 4 m thick. Layer 3 is located at depths > 20 m at begining of the profile and about 10 m at the profile end.

4.4.11 Profile Eleven

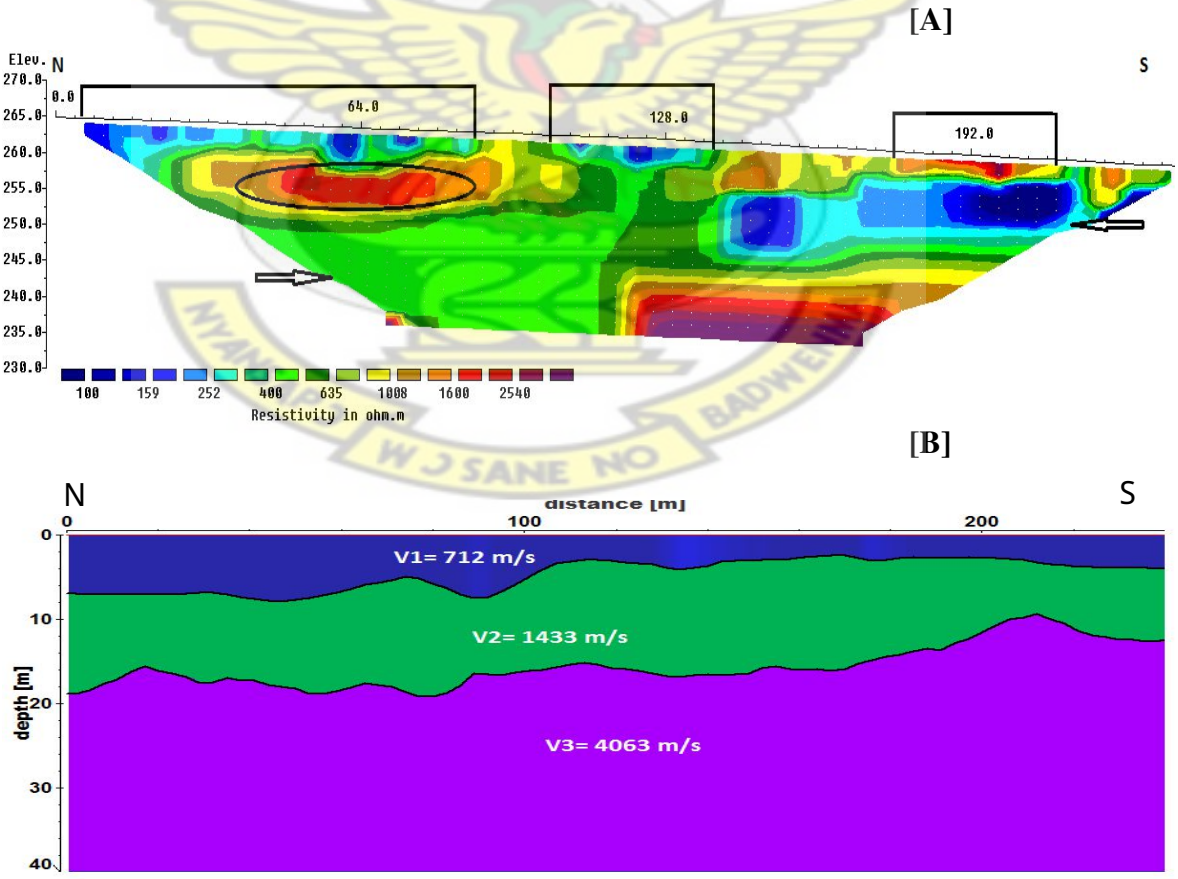

Figure 4.14: 2D apparent resistivity model section and velocity-depth model of profile 11.

The subsurface to depth of 5 m of the apparent resistivity model section for line 11 (figure 4.14 [A]) displays low resistivity (< 600 Ω.m) from the begining of the profile to 140 meters. Below this zone is a confined high resistive region (> 1500 Ω.m) in the subsurface about 7 m thick. This highly resistive zone has a sharp reduction in resistivity (< 600 Ω.m) at deeper depths. The subsurface from 140 meters to the end of the profile show high resistivity to depth of 7 m. This region is followed by a 10 m thick low resistive zone (< 600 Ω.m) which also precedes a very high resistive region (> 1500 Ω.m).

On the velocity-depth model of line 11 (figure 4.14 [B]), layers 1, 2 and 3 recorded average velocities of 712 m/s, 1433 m/s and 4063 m/s respectively. Layer 1 is about 7 m thick from the begining of the line to 100 meters and 4 m thick from 100 meters to the end of the line. Layer 3 was delineated at depths > 16 m averagely.

4.4.12 Profile Twelve

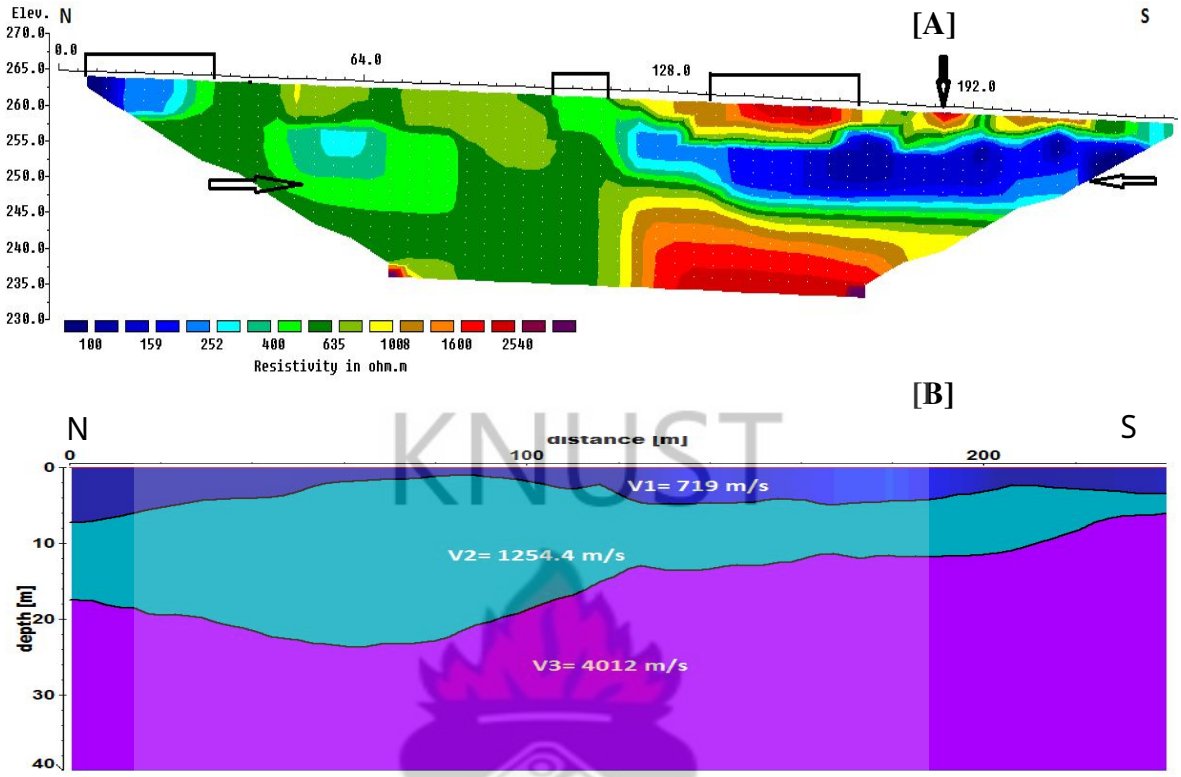

Figure 4.15: 2D apparent resistivity model section and velocity-depth model of profile 12.

Low resistive zones (< 600 Ω.m) on the apparent resistivity model section of line 12 (figure 4.15 [A]) are located from the begining of the line to 44 meters that extends to depths of 26 m in the subsurface. From 120-220 meters of the subsurface to depths of 6 m shows high resistivity (> 700 Ω.m) underlain by a very low resistive zone (< 200 Ω.m) 12 m thick which extends to the end of the line. This very low resistive zone is seated on a very high resistive zone (> 1008 Ω.m).

The velocity-depth model of line 12 (figure 4.15 [B]) has an average velocity of 719 m/s and thickness of about 4 m for layer 1. Layer 2 and 3 have average velocities of 1254.4 m/s and 4012 m/s respectively. Layer 3 is 14 m deep from 120 meters to the end of the profile but was delineated at depths > 18 m from the begining of the line to 120 meters.

4.4.13 Profile Thirteen

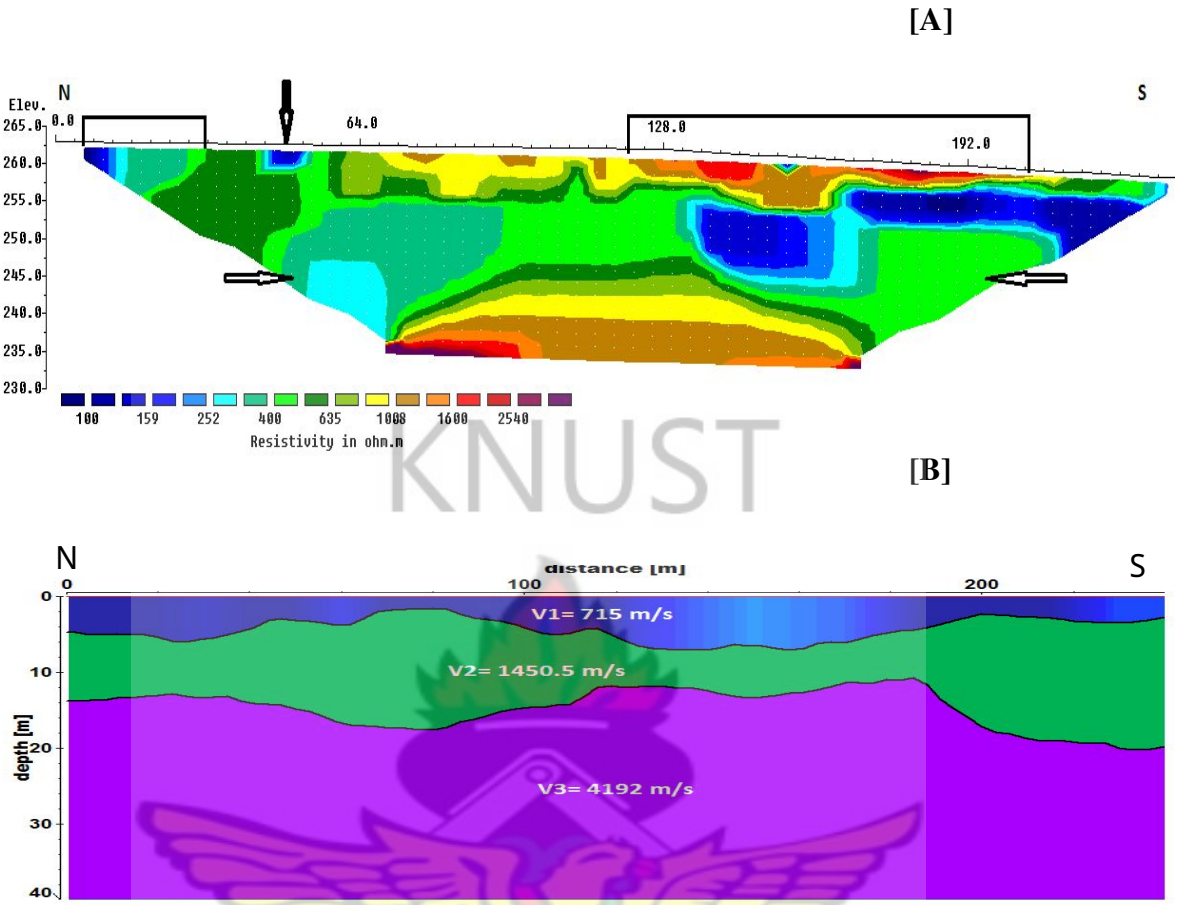

Figure 4.16: 2D apparent resistivity model section and velocity-depth model of profile 13.

The apparent resistivity model section of line 13 (figure 4.16 [A]) displays high resistivity (> 700 Ω.m) in the subsurface from 68-120 meters to depths of about 7 m. This high resistive zone is bouded by a region of low resistivity to depths of about 20 m in the subsurface. From 20-27 m depth of this resistivity model section has resistivities of about 700-1500 Ω.m.

On the velocity-depth model of line 13 (figure 4.16 [B]), layer 1 recorded and average velocity of 715 m/s with thickness of about 5 m. Layer 2 and 3 recorded average velocities of 1450.5 m/s and 4192 m/s respectively. Layer 3 is located at depths > 14 m at the begining of the line and > 20 m close to the end of the line from 180-240 meters.

4.4.14 Profile Fourteen

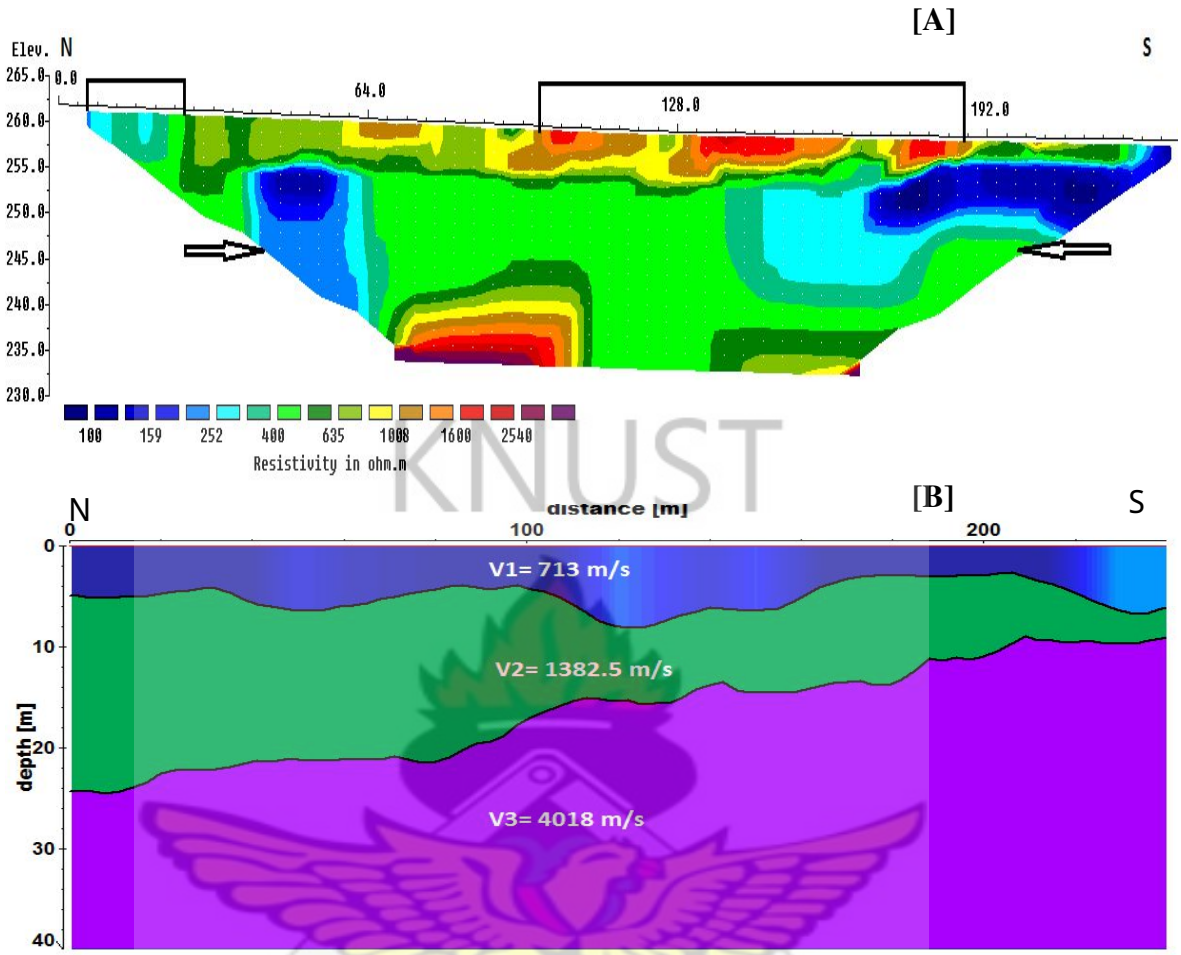

Figure 4.17: 2D apparent resistivity model section and velocity-depth model of profile 14.

The 2D apparent resistivity model section of line 14 (figure 4.17 [A]) displays very high resistivity in the subsurface from 64 to 192 meters to 7 m depth. The central portions of this model section is dominated by low resistivity (< 500 Ω.m).

Layer 1 of the velocity-depth model of profile 14 (figure 4.17 [B]) has a thickness of 6 m recording an average velocity of 715 m/s. Layers 2 and 3 recorded average velocities of 1382.5 m/s and 4018 m/s respectively. The third layer slopes gently from the end of the profile at 12 m to the begining at 24 m.

4.4.15 3D resistivity model

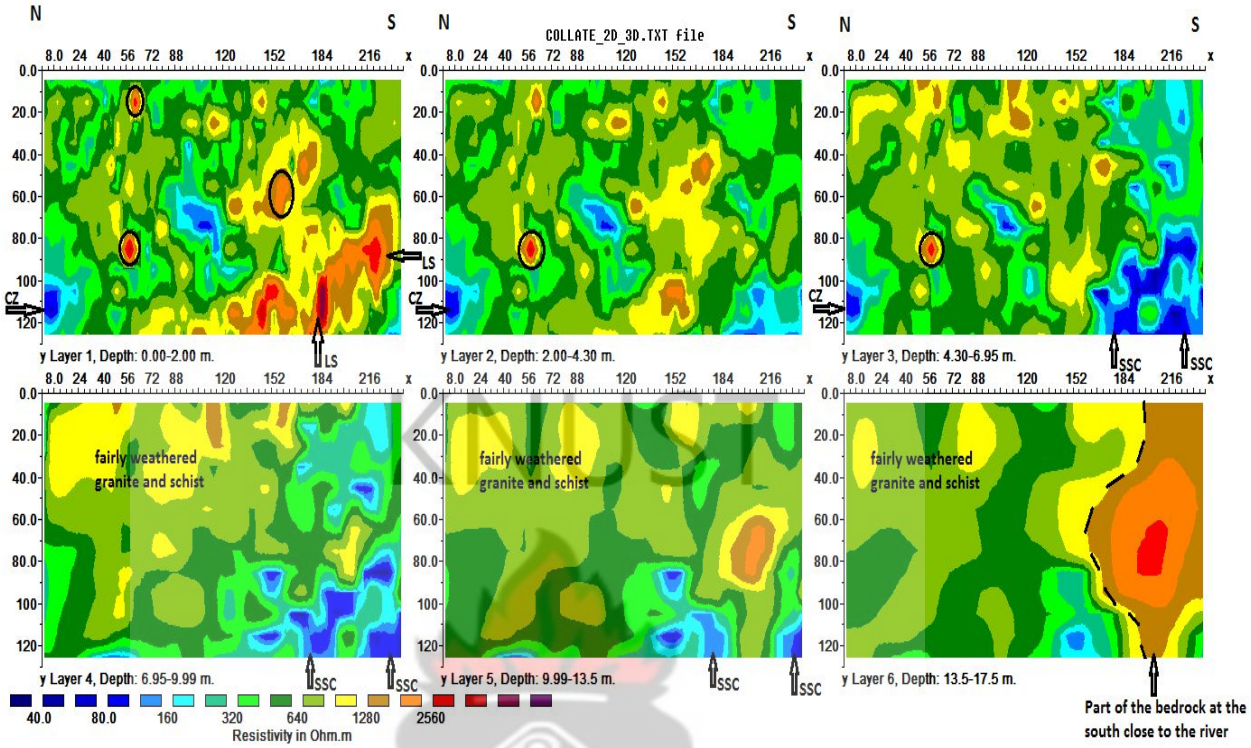

Figure 4.18: Six slices of a 3D resistivity model of the underground.

Figure 4.18 shows slices of a 3D resistivity model of the underground. The first layer at depth of 2 m shows parts at the North marked as clay zones (CZ) with resistivities < 400 Ω.m. This formation is also encountered at the same positions on the model for layers 1, 2, 3 and disappears on layers 4, 5 and 6 at deeper depth. High resistivities (> 1500 Ω.m) encountered at the Southwest part on slice 1, could be dry and disseminated sand (LS). The parts circled on layers 1, 2 and 3 of the model probably are air-filled voids. From 184-240 m at the Southern part of layers 2, 3 and 4 has dominant resistivities < 500 Ω.m probably due to the presence of sandy-clay. At depth of 7-17 m considering layers 4, 5 and 6 at the Northeast, the subsurface displays high resistivities > 640 Ω.m reflecting a compact subsurface at that region. The parts marked SSC with resistivities < 200 Ω.m on layers 2, 3, 4 and 5 are probably resulting from saturated sandy-clay. On layer 6 occuring at depth 17.5 m from 184

m to the end of the profile is a highly resistive region which probably is part of the underlying bedrock. It can be deduced that the bedrock is located at a shallow depth in the subsurface > 13.5 m at the South.

4.5 Discussion of Results

As a result of compaction, materials beneath the Earth surface have increasing velocity and resistivity with increasing depths. Elastic wave velocity and apparent resistivity are essential rock parameters from which the geotechnical engineer can deduce the rippability of rocks. A rock that can be ripped with less difficulty is partly weathered. Weathered rocks have low seismic velocities and resistivities.

Loose and disseminated soils sometimes have p-wave velocities as low as the velocity of sound in air (Milsom, 2007). The first layer revealed by the seismic data is interpretated to be the topsoil. An average velocity of 782.22 m/s and 711.6 m/s for profiles 1-9 and 10-14 respectively were recorded for the topsoil. The velocity difference suggest that the topsoil for lines 1-9 (east) is a little compact than that of lines 10-14 (west). The subsurface to depth of about 5 m for profiles 1-9 show dominant moderately high to high resistivities > 500 Ω.m suggesting a compact topsoil. The subsurface to depth of 5 m of profiles 10-14, from the middle to the end of the lines, have very high resistivities (> 1600 Ω.m) which probably is as a result of laterite and mixture of dry loose sand and alluvium. Disseminated sediments have high porosity with air if dry. The presence of air in these sediments results in very high resistivities. From the midpoint to the begining of profiles 10-14, the subsurface to depth of 5 m have resistivities < 500 Ω.m also suggesting less compact topsoil at the west of the study area.

Second layer of the velocity-depth models is a weathered zone.

The weathered zone (layer 2) has p-wave velocities between 1189 m/s and 1450 m/s. Layer 2 for profiles 10-14 has a little high velocities (1200-1450 m/s) which may be the influence of water. Compact zones have high resistivities. The subsurface for lines 1-9 have high resistivities > 650 Ω.m which suggest a compact weathered zone. On profiles 10-14, the weathered zone have dominant resistivities < 500 Ω.m indicating a highly weathered zone. Weathering reduces compaction by increasing pore content.

The depth to the third layer on line 10-14 suggests less compact subsurface at the west side of the project site leading fast attenuation of the seismic waves. A close examination of the velocities with depth, shows higher velocities at deeper depths and also the occurence of layer 3 close to the surface on the southern parts of the study area (figure 4.19). Layer three is the underlying hard rock with velocities in the range of non rippable granitic formation. A survey by Milsom (2007) showed granite with velocity 3800 m/s not rippable. Also Bell et al. (1992) found out in his work some granitic formation with velocity a little > 1800 m/s which could not be ripped by a D-9 tractor. Layer three has velocities > 3759 m/s.

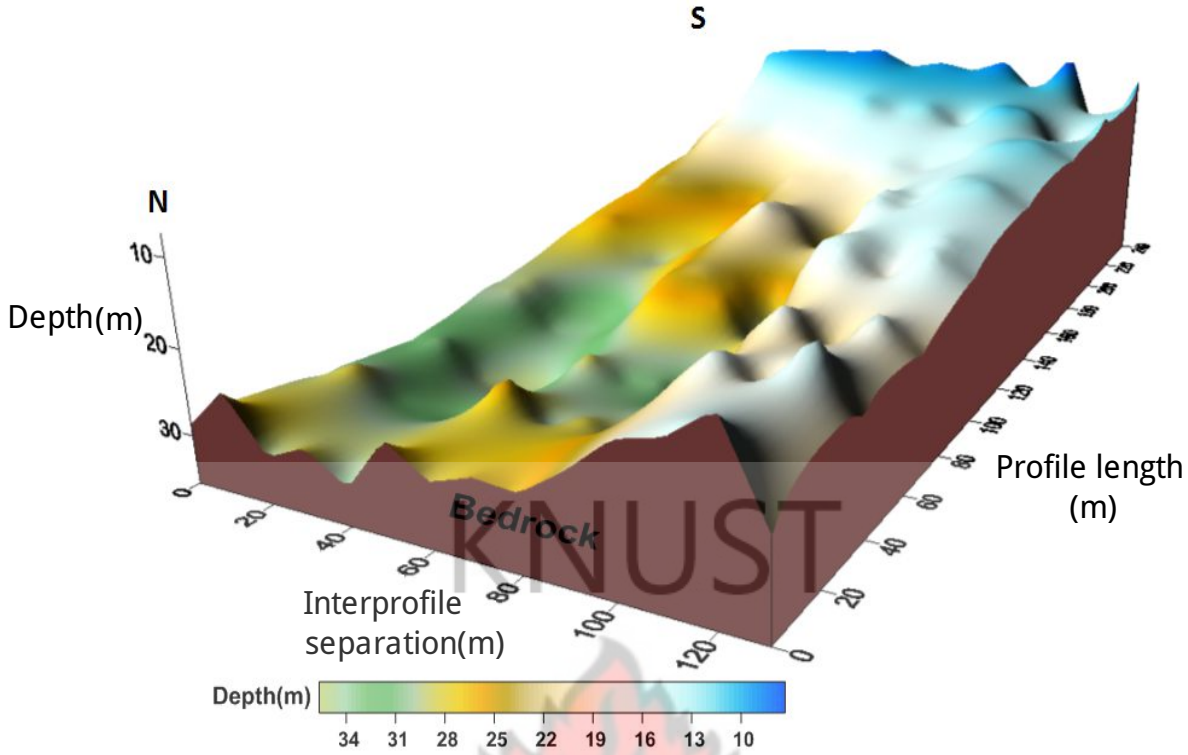

Figure 4.19: 3D model of the top of the bedrock.

Fissures are cracks that provide room for hydrothermal fluids, air or water and are characterized by very small regions with sharp resistivity contrast depending on the fluid chemistry. Also sharp resistivity contrast zones that appear as thin lines within formations on 2D resistivity models are faults (Aning et al., 2013). Faulted zone can also be identified as a continuous formation with a sharp slip up or down on a 2D resistivity model section.

Very high confined resistivity zones on resistivity model sections deviates from normal geologic formations and represent air-filled voids (Sheets, 2002). Part of the subsurface on profiles 1, 2, 3, 4, 5, 6, 10 and 11 have confined high resistivities that probably might be resulting from voids filled with and air. The presence of water or clay cause low resistivities on 2D resistivity models. Part of the subsurface has very low resistivities < 250 Ω.m which may be the cause of clay or water. This very low resistivities in the subsurface occur mostly on the southern and western parts.

CHAPTER 5

CONCLUSIONS AND RECOMMENDATIONS

5.1 Conclusions

Integrating dc resistivity and seismic refraction methods provides one of the effective means of environmental studies in geophysics. The physical properties, resistivity and p-wave velocity, help in making reliable inferences about the nature of the subsurface for the purpose of construction. In this work, the main focus was using refraction seismics and resistivity methods to image the subsurface to locate the presence of voids, fissures and faults, in addition examine the compaction of the weathered zone and find the depth to the bedrock.

Under different surface conditions, the mineral composition of a rock is transformed by virtue of biogeochemical hydrolysis (Tardy, 1971; Olona et al., 2010b). This process is referred to as weathering. In a granitic environment especially, this process together with alteration have a basic effect on their geotechnical properties such as p-wave velocity and resistivity (Dewandel et al., 2006; Olona et al., 2010b; Begonha and Braga, 2002; Lan et al., 2003). This makes it neccessary to investigate a site prior to construction as alteration, weathering and other rock properties may be irregularlly distributed in a bedrock.

To depth of about 7 m from profile 1 to 9 in the subsurface on the east and north show very good compaction and become less compact from line 10 to 14. Resistivity > 1600 Ω.m found in the subsurface to depths of about 3 m close to the end of the profiles at the south is as a

result of mixture of loose sand alluvium deposits. The subsurface to 7 m depth for profile 1 to 9 display moderately high resistivities > 600 Ω.m. Below depths of about 5 m from profile 10-14 in the subsurface, the 2D apparent resistivity model sections display dominant low resistivities < 500 Ω.m that suggest a highly weathered underground incompetence in supporting the weight of giant buildings. The weathered zone (layer 2) for the velocity-depth models show decreasing thickness from north to south. Confined high resistivity regions (> 1500 Ω.m) below depths of about 5 m encountered on lines 1, 2, 4, 5, 10 and 11, strongly could be voids filled with air.

The seismic method delineated the hard underlying bedrock at varying depths (17-32 m). The bedrock was found at deeper depth of > 24 m at the north with an up-dip in the southern direction about 17 m from the surface which could not be clearly mapped by the resistivity method. A sharp down slip in the bedrock on the velocity-depth model of profile 13 from 180 meters to the end of the profile suggest a fault in that region.

The 2D electrical resistivity method is very reliable in delineating low resitive formations sandwiched between highly resistive regions and even patches of less resistive boulders within the matrix of a rock formation. The subsurface of lines 1-9 has resistivities > 600 Ω and an average elastic wave velocities of 782.22 m/s, 1261.7 m/s and 4497 m/s for layers 1, 2 and 3 respectively which indicate a competent subsurface for contruction purposes. For lines 10-14, the subsurface has resistivities < 500 Ω and an average p-wave velocity of 711.6 m/s, 1346.34 m/s and 4008.8 m/s for layer 1, 2 and 3 respectively reflecting a less competent subsurface for the purpose of construction.

Generally, the subsurface is made of clay, sandy-clay, fairly weathered granite and schist, laterite, dry loose sand and alluvium deposits.

5.2 Recommendations and Future Work

These recommendations were made based on the results and discussions, critical examination of the resistivity model sections and seismic velocities obtained from the underground models and the external features found on the study area, mostly anthills and dry superficial deposits.

1. The subsurface to a meter depth should be be graded off before construction. This will help take off part of the subsurface dominantly made of laterite and loose sand to expose a hard surface.

2. The subsurface at the southern parts is highly weathered and buildings at that part may possibly submerge. Inview of this, that side should be used as a parking lot.

3. Seismic refraction and resistivity surveys should be carried out on cross profiles at the site to compare information at points of intersection of the profiles.

References

1. Ahmad, J., Schmitt, D. R., Rokosh, C. D., and Pawlowicz, J. G. (2009). High-resolution seismic and resistivity profiling of a buried quaternary subglacial valley: Northern Alberta, Canada. *Geological Society of America Bulletin*, 121(11-12):1570–1583.

2. Ahmed, JaddoaAl-Heety & Nabil, A.-S. H. (2014). Seismic refraction tomography & MASW survey for geotechnical evaluation of soil for the Teaching Hospital project at Mosul university.

3. Aizebeokhai, A. P. (2010). 2d and 3d geoelectrical resistivity imaging: theory and field design. *Scientific Research and Essays*, 5(23):3592–3605.

4. Aizebeokhai, A. P., Olayinka, A., and Singh, V. (2010). Application of 2d and 3d geoelectrical resistivity imaging for engineering site investigation in a crystalline basement terrain, southwestern nigeria. *Environmental Earth Sciences*, 61(7):1481–1492.

5. Amidu, S. and Olayinka, A. (2006). Environmental assessment of sewage disposal systems using 2d electrical-resistivity imaging and geochemical analysis: A case study from Ibadan, southwestern Nigeria. *Environmental & Engineering Geoscience*, 12(3):261–272.

6. Andrews, N., Aning, A., Danuor, S., and Noye, R. (2013). Geophysical investigations at the proposed site of the knust teaching hospital building using 2d and 3d resistivity imaging techniques. *Int. Res. Jour. Geol. Min*, 3(3):113–123.

7. Aning, A., Sackey, N., Jakalia, I., Sedoawu, O., Tetteh, E., Hinson, G., Akorlie, R., Appiah, D., and Quaye, E. (2014). Electrical resistivity as a geophysical mapping tool; A case study of the new Art Department, KNUST-Ghana. *International Journal of Scientific & Research Publications*, 4.

8. Aning, A. A., Tucholka, P., and Danuor, S. K. (2013). 2d electrical resistivity tomography (ert) survey using the multi-electrode gradient array at the Bosumtwi impact crater, Ghana. *Journal of Environment & Earth Science*, 3(5).

9. Begonha, A. and Braga, S. (2002). Weathering of the Oporto granite: geotechnical and physical properties. *Catena*, 49(1):57–76.

10. Bell, F. G. et al. (1992). *Engineering properties of soils and rocks.* Number Ed. 3. Butterworth-Heinemann Ltd.

11. Benson, R., Glaccum, R. A., and Noel, M. R. (1984). Geophysical techniques for sensing buried wastes and waste migration. In *Geophysical techniques for sensing buried wastes and waste migration*. EPA.

12. Benson, R. and Yuhr, L. (2002). Site characterization strategies: old and new. In *Second Annual Conference on the Application of Geophysical and NDT Methodologies to Transportation Facilities, Federal Highway Ad-ministration, April*, pages 15–19.

13. Benson, R., Yuhr, L., and Kaufmann, R. (2003). Some considerations for selection and successful application of surface geophysical methods. In *the 3rd International Conference on Applied Geophysics, Hotel Royal Plaza, Orlando, Florida*.

14. Benson, R. C. and Yuhr, L. (1995). Geophysical methods for environmental assessment. In *Geoenvironment 2000@ sCharacterization, Containment, Remediation, and Performance in Environmental Geotechnics*, pages 57–76. ASCE.

15. Bentley, L. R. and Gharibi, M. (2004). Two-and three-dimensional electrical resistivity imaging at a heterogeneous remediation site. *Geophysics*, 69(3):674–680.

16. Bommer, J., Rolo, R., Mitroulia, A., and Berdousis, P. (2002). Geotechnical properties and seismic slope stability of volcanic soils. In *Proceedings of the 12th European Conference on Earthquake Engineering, London*.

17. Bommer, J. J. and Rodriguez, C. E. (2002). Earthquake-induced landslides in central America. *Engineering Geology*, 63(3):189–220.

18. Butler, D. K. (2005). *Near-surface geophysics*. Society of Exploration Geophysicists Tulsa.

19. Campbell, RB and Bower, CA and Richards, LA. (1948). Change of electrical conductivity with temperature and the relation of osmotic pressure to electrical conductivity and ion concentration for soil extracts. Soil Sci. Soc. Am. Proc. 13.

20. Cecil, OS (1971). Correlation of seismic refraction velocities and rock support requirements in Swedish tunnels. Swedish Geotechnical Inst Reprints & Repts.

21. Colella, A., Lapenna, V., and Rizzo, E. (2004). High-resolution imaging of the high Agri valley basin (southern Italy) with electrical resistivity tomography. *Tectonophysics*, 386(1):29–40.

22. Coskun, N. (2012). The effectiveness of electrical resistivity imaging in sinkhole investigations. *International Journal of Physical Sciences*, 7(15):2398–2405.

23. Cox, M. J., Scherrer, E. F., and Chen, R. (1999). Static corrections for seismic reflection surveys.

24. Dahlin, T. and Loke, M. H. (1998). Resolution of 2d wenner resistivity imaging as assessed by numerical modelling. *Journal of Applied Geophysics*, 38(4):237–249.

25. Dahlin, T. and Zhou, B. (2004). A numerical comparison of 2d resistivity imaging with 10 electrode arrays. *Geophysical prospecting*, 52(5):379–398.

26. Dewandel, B., Lachassagne, P., Wyns, R., Maréchal, J., and Krishnamurthy, N. (2006). A generalized 3-d geological and hydrogeological conceptual model of granite aquifers controlled by single or multiphase weathering. *Journal of Hydrology*, 330(1):260–284.

27. Diaferia, I., Barchi, M., Loddo, M., Schiavone, D., and Siniscalchi, A. (2006). Detailed imaging of tectonic structures by multiscale earth resistivity tomographies: The Colfiorito normal faults (central Italy). *Geophysical Research Letters*, 33(9).

28. Dutta, N. (1984). Seismic refraction method to study the foundation rock of a dam. *Geophysical prospecting*, 32(6):1103–1110.

29. Gharibi, M. and Bentley, L. R. (2005). Resolution of 3-d electrical resistivity images from inversions of 2-d orthogonal lines. *Journal of Environmental & Engineering Geophysics*, 10(4):339–349.

30. Giocoli, A., IMAA-CNR, T. S. P., Magrì, C., Vannoli, P., Piscitelli, S., IMAA-CNR, T. S. P., Rizzo, E., IMAA-CNR, T. S. P., Siniscalchi, A., Burrato, P. (2007). Electrical resistivity tomography investigations in the Ufita valley (southern Italy). *Annals of Geophysics*.

31. Goldstein, N. E. (2009). Expedited site characterization geophysics: geophysical methods and tools for site characterization.

32. Gremaud, P.A and Kuster, C.M. (2006). Computational study of fast methods for the eikonal equation. *SIAM journal on scientific computing*, 27(6):1803–1816.

33. Griffiths, D. and Barker, R. (1993). Two-dimensional resistivity imaging and modelling in areas of complex geology. *Journal of Applied Geophysics*, 29(3):211–226.

34. GSD. (2009). *Geological Map of Kumasi Metropolis*.

35. Habberjam, GM and Watkins, GE. (1967). The use of a square configuration in resistivity prospecting. Geophysical prospecting.

36. Hatherly, P. and Neville, M. (1986). Experience with the generalized reciprocal method of seismic refraction interpretation for shallow engineering site investigation. *Geophysics*, 51(2):255–265.

37. Junner, N. (1940). *Geology of the Gold Coast and Western Togoland (with revised geological map).* Gold Coast Geological Survey Bulletin. 11, 40p, Accra.

38. Kearey, P. and Brooks, M. (2002). An introduction to geophysical exploration. *Blackwell Publishing, ISBN*, 978(0):632.

39. Kearey, P., Brooks, M., and Hill, I. (2009). *An introduction to geophysical exploration*. John Wiley & Sons.

40. Keller, George Vernon and Frischknecht, Frank C. (1966). Electrical methods in geophysical prospecting. Pergamon

41. Kesse, G. (1985). *Minerals and rocks resources of Ghana*.

42. Khan, M. Y. (2013). Engineering geophysical study of unconsolidated top soil using shallow seismic refraction & electrical resistivity techniques. *Journal of Environment & Earth Science*, 3(8):120–127.

43. Kilty, K. T., Norris, R. A., McLamore, W. R., Hennon, K. P., and Euge, K. (1986). Seismic refraction at horse mesa dam: An application of the generalized reciprocal method. *Geophysics*, 51(2):266–275.

44. Kohnen, H. (1974). The temperature dependence of seismic waves in ice. *J. Glaciol*, 13(67):144–147.

45. Lan, H., Hu, R., Yue, Z., Lee, C., and Wang, S. (2003). Engineering and geological characteristics of granite weathering profiles in south china. *Journal of Asian Earth Sciences*, 21(4):353–364.

46. Loke, M. (2001). Tutorial: 2-d and 3-d electrical imaging surveys. *Copyright (1996-2012)*.

47. Lowrie, W. (1997). *Fundamentals of geophysics*. Cambridge University Press.

48. Milsom, J. (2007). *Field geophysics*, volume 25. John Wiley and Sons.

49. Moustafa, S. S., Ibrahim, E. H., Elawadi, E., Metwaly, M., and Al Agami, N. (2012). Seismic refraction and resistivity imaging for assessment of groundwater seepage under a dam site, southwest of saudi arabia. *International Journal of Physical Sciences*, 7(48):6230–6239.

50. Olayinka, A. and Yaramanci, U. (1999). Choice of the best model in 2-d geoelectrical imaging: case study from a waste dump site. *European Journal of Environmental and Engineering Geophysics*, 3:221–244.

51. Oldenborger, G. A., Routh, P. S., and Knoll, M. D. (2005). Sensitivity of electrical resistivity tomography data to electrode position errors. *Geophysical Journal International*, 163(1):1–9.

52. Olona, J., Pulgar, J. A., Fernandez-Viejo, G., Lopez-Fernandez, C., and Gonzalez-Cortina, J. M. (2010a). Weathering variations in a granitic massif and related geotechnical properties through seismic and electrical resistivity methods. *Near Surface Geophysics*, 8(6):585–599.

53. Olona, J., Pulgar, J. A., Fernandez-Viejo, G., Lopez-Fernandez, C., and Gonzalez-Cortina, J. M. (2010b). Weathering variations in a granitic massif and related geotechnical properties through seismic and electrical resistivity methods. *Near Surface Geophysics*, 8(6):585–599.

54. Osazuwa, I. and Chii, E. C. (2010). Two-dimensional electrical resistivity survey around the periphery of an artificial lake in the precambrian basement complex of northern nigeria. *International Journal of Physical Sciences*, 5(3):238–245.

55. Palmström, A. (1996). Application of seismic refraction stjrvey in assessment of jointing.

56. Revil, A and Glover, PWJ. (1997). Theory of ionic-surface electrical conduction in porous media. Physical Review B.

57. Reynolds, J. M. (2011). *An introduction to applied and environmental geophysics*. John Wiley & Sons.

58. Robert, J. G., Barning, K., Francis, L. A., and Fred, K. A. (2002). *Gold Deposites of Ghana*. Gandalf Graphics Limited, 605 Alden Rd., Markham, Ontario, Canada.

59. Rucker, M. L. (2000). Applying the seismic refraction technique to exploration for transportation facilities. *Geophysics*, 1:1–3.

60. Sandmeier, J.K (2008). WindowsâĎć 9x/NT/2000/XP-program for the processing of seismic, acoustic or electromagnetic reflection, refraction and transmission data.

61. Sethian, James A and Vladimirsky, Alexander, (2000). Fast methods for the Eikonal and related Hamilton–Jacobi equations on unstructured meshes. *Proceedings of the National Academy of Sciences*, 97(11):5699–5703.

62. Scollar, I., Tabbagh, A., Hesse, A., and Herzog, I. (1990). *Archaeological prospecting and remote sensing*. Cambridge University Press.

63. Senos Matias, MJ. (2002). Square array anisotropy measurements and resistivity sounding interpretation. Journal of Applied Geophysics.

64. Sheets, R. A. (2002). Use of electrical resistivity to detect underground mine voids in Ohio.

65. Sheriff, R. E. (2002). Encyclopedic dictionary of applied geophysics.

66. Sjögren, B. (1984). *Shallow refraction seismics*. Chapman and Hall London.

67. Sjøgren, B., Øfsthus, A., and Sandberg, J. (1979). Seismic classification of rock mass qualities*. *Geophysical Prospecting*, 27(2):409–442.

68. Soupios, P., Georgakopoulos, P., Papadopoulos, N., Saltas, V., Andreadakis, A., Vallianatos, F., Sarris, A., and Makris, J. (2007). Use of engineering geophysics to investigate a site for a building foundation. *Journal of Geophysics and Engineering*, 4(1):94.

69. Tardy, Y. (1971). Characterization of the principal weathering types by the geochemistry of waters from some european and african crystalline massifs. *Chemical Geology*, 7(4):253–271.

70. Telford, W. M. and Sheriff, R. E. (1990). *Applied geophysics*, volume 1. Cambridge university press.

71. Ugwu, G. Z. and Ezema, P. O. (2013). 2d electrical resistivity imaging for the investigation of the subsurface structures at the proposed site for kauridan estate at ibagwa–nike, southeastern nigeria. *Article Author (s) page*, page 528.

72. Ushie, Fedelis & Eminue, O. (2013). Seismic refraction profiling for groundwater in a

basement terrain: The case of Akamkpa, Southeast Nigeria. *Journal of Environment and Earth Science*, 3(14):195–200.

73. Varnes, D. (1978). Slope movements types and processes, schuster rl & krizek rj ed.-landslide, analysis and control. *Transportation Research Board Sp. Rep*, (176).

74. Ward, Stanley H. (1990). Resistivity and induced polarization methods. Geotechnical and environmental geophysics

75. www.goggle.com/ghana/districts/kma. (2014). Climatic condition of Kumasi metropolis.

76. www.knust.edu.gh (2014). Guide map of Kwame Nkrumah University of Science and Technology.

77. www.wikipedia.org/wiki/Eikonal_equation, (2014). Eikonal equation.

78. Wyllie, M., Gregory, A., and Gardner, G. (1958). An experimental investigation of factors affecting elastic wave velocities in porous media. *Geophysics*, 23(3):459–493.

79. Yilmaz, S. (2011). A case study of the application of electrical resistivity imaging for investigation of a landslide along the highway. *Int J Phys Sci*, 6(24):5843–5849.

80. Zhou, B. and Dahlin, T. (2003). Properties and effects of measurement errors on 2d resistivity imaging surveying. *Near Surface Geophysics*, 1(3):105–117.

Appendix A

A.1 Layer velocities on the various profiles.

Table A.1: Primary wave velocity of the various layers on each profile.

Profile No.	Average p-wave velocity (m/s)		
	Layer 1	Layer 2	Layer 3
1	870	1206.7	5321
2	747	1189.1	4817
3	795	1349.5	4678
4	816	1207.3	5016
5	815	1273	4245
6	734	1211.1	3943
7	754	1252.1	4009
8	704	1287	4139
9	805	1379.5	4305
10	699	1211.3	3759
11	712	1433	4063
12	719	1254.4	4012
13	715	1450.5	4192
14	713	1382.5	4018

Appendix B

B.1 Used Softwares

- MapInfo : Location Map of study area.
- ReflexW version 7: Seismic data processing and modelling.
- ArcGis: Geologic Map of study area.
- Res2D INV : Processing of resistvity data.
- LaTeX: Typesetting and layout
- Golden Software Grapher 10 : X-T graph plots.
- Microsoft Paint: Ehancement of velocity-depth and 2D resistvity models.